

ThesisTitle

by

Daniel C. Cole

Other Degrees

A thesis submitted to the
Faculty of the Graduate School of the
University of Colorado in partial fulfillment
of the requirements for the degree of
Doctor of Philosophy
Physics Physics
2018

This thesis entitled:
ThesisTitle
written by Daniel C. Cole
has been approved for the Physics Physics

Reader1

Reader2

Date _____

The final copy of this thesis has been examined by the signatories, and we find that both the content and the form meet acceptable presentation standards of scholarly work in the above mentioned discipline.

Cole, Daniel C. (Ph.D., Physics)

ThesisTitle

Thesis directed by Dr. Scott A. Diddams

Optical frequency combs have revolutionized precision metrology by enabling measurements of optical frequencies, with implications both for fundamental scientific questions and for applications such as fast, broadband spectroscopy. In this thesis, I describe the development of comb generation platforms with smaller footprints and higher repetition rates, with the ultimate goal of bringing frequency combs to new applications in a chip-integrated package. I present two new types of frequency combs: electro-optic modulation (EOM) combs and Kerr-microresonator-based frequency combs (microcombs). First I describe the EOM comb scheme and, in particular, techniques for mitigating noise in the comb generation process, and I present the results of a proof-of-principle metrology experiment and some possible applications. Then I discuss developments in microcomb technology. I present novel ‘soliton crystal’ states, which have highly structured ‘fingerprint’ optical spectra that correspond to ordered pulse trains exhibiting crystallographic defects. These pulse trains arise through interaction of the solitons with avoided mode-crossings in the resonator spectrum. Next, I describe the direct and deterministic generation of single microresonator solitons using a phase-modulated pump laser. This technique removes the dependence on initial conditions that was formerly a universal feature of these experiments, presenting a solution to a significant technical barrier to the practical application of microcombs. I also discuss generation of Kerr combs in the Fabry-Perot (FP) geometry. I introduce a nonlinear partial differential equation describing dynamics in an FP cavity and discuss the differences between the FP geometry and the ring cavity, which is the geometry used in previous Kerr-comb experiments. Finally, I discuss a technique for reducing the repetition rate of a high-repetition-rate frequency comb, which will be a necessary post-processing step for some applications. I conclude with a discussion of avenues for future research, including the chip-integration of Fabry-Perot Kerr resonators and the use of band-engineered photonic crystal cavities to further simplify soliton generation.

Acknowledgements

The work in this thesis would not have been possible...

- Acknowledgement line 1
- Acknowledgement line 2

Contents

1	Introduction to microresonator-based frequency combs	1
1.1	Optical microring resonators	1
1.1.1	Resonant enhancement in a microring resonator	4
1.1.2	Thermal effects in microresonators	5
1.2	Microring resonator Kerr frequency combs	7
1.3	A model for Kerr-comb nonlinear optics: The Lugiato-Lefever equation	9
1.4	Analytical investigation of the resonator's CW response	12
1.5	Kerr comb outputs: extended modulation-instability patterns	15
1.6	Kerr comb outputs: solitons	16
1.6.1	Experimental generation of solitons	19
2	Pulse Picking	22
2.1	Proof-of-Concept Experiment	23
2.2	Mathematical model for downsampling	25
2.3	Experimental investigation of the effect of downsampling on the pulse train's noise properties	27
2.4	Effects of ideal downsampling on a pulse train's noise properties	29
2.5	Model for the effect of incomplete extinction of rejected pulses and amplification of a downsampled pulse train	32
2.6	Further remarks on the application of downsampling	35

References**37**

Figures

1.1	Optical microdisk resonator	2
1.2	Thermal bistability in microresonators	7
1.3	An illustration of four-wave mixing and frequency-comb generation.	8
1.4	Solution space for the Lugiato-Lefever equation	12
1.5	Investigation of the circulating CW power in a Kerr resonator	14
2.1	An illustration of pulse-train repetition-rate downsampling	23
2.2	Demonstration of downsampling for f_0 detection	25
2.3	Experimental investigation of noise introduced by downsampling	28
2.4	Effect of downsampling on photocurrent fluctuations	32
2.5	Investigation of incomplete pulse extinction and amplification	35

Chapter 1

Introduction to microresonator-based frequency combs

This chapter introduces the basic physics of optical frequency-comb generation in Kerr-nonlinear microresonators, with an emphasis on providing context for the results described in the subsequent chapters. A number of papers that review the topic have been published, each of which provides a unique perspective on this rapidly evolving field [1–4].

For simplicity, and following the terminology of the field, we will refer to broadband optical spectra generated through frequency conversion in Kerr-nonlinear resonators as ‘Kerr combs,’ even when the output is not strictly a coherent frequency comb. So far researchers have focused on Kerr-comb generation using microresonators with a ring geometry—so-called microring resonators. It is also possible to generate Kerr combs in a Kerr-nonlinear Fabry-Perot (FP) cavity, as has been recently demonstrated by Obrzud, Lecomte, and Herr [5]. Theoretical investigations of Kerr-comb generation with the FP geometry are presented in Chapter ??.

1.1 Optical microring resonators

An optical microring resonator guides light around a closed path in a dielectric medium by total internal reflection. The principle is the same as the guiding of light in an optical fiber, and indeed a ‘macroring’ resonator can be constructed from a loop of fiber, using a fiber-optic coupler with a small coupling ratio as an input/output port. Ring resonators are often referred to as whispering-gallery mode resonators due to the similarity between their guided modes and the acoustic ‘whispering-gallery’ waves that permit a listener on one side of St. Paul’s cathedral (for example) to hear

whispers uttered by a speaker on the other side of the cathedral, as explained by Lord Rayleigh beginning in 1910. A schematic depiction of the basic components of a typical microring-resonator experiment is shown in Fig. ?? . Optical microring resonators have a host of characteristics that make them useful for nonlinear optics and photonics applications; these include the ease with which they can be integrated, the ultra-high quality (Q) factors that have been demonstrated, and the ability to tailor the spectral distribution of guided modes through careful resonator design.

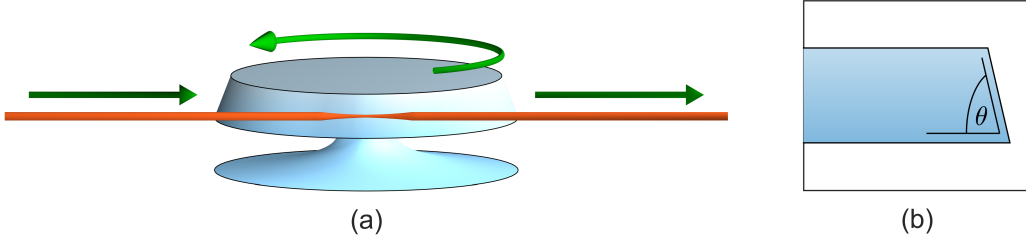


Figure 1.1: **Optical microdisk resonator.** (a) An optical microring resonator with the disk geometry as described in Ref. [6], operated in a through-coupled configuration. Light is evanescently coupled into and out of the resonator through a tapered optical fiber, shown in orange, which contacts the resonator near the fiber's point of smallest diameter. Light circulates in whispering-gallery modes concentric to the resonator's circumference. (b) The wedge angle θ can be adjusted to control the geometric dispersion of the propagating whispering-gallery modes as described in Ref. [7], as θ dictates, for example, the extent to which larger (longer-wavelength) modes are confined further from the circumference of the wedge.

A microring resonator supports propagating guided optical modes of electromagnetic radiation with (vacuum) wavelengths that evenly divide the optical round-trip path length: $\lambda_m = n_{eff}(\lambda_m)L/m$, with associated resonance frequencies $\nu_m = c/\lambda_m = mc/n_{eff}(\nu_m)L$. This leads to constructive interference between the circulating field and the input field. Here L is the physical circumference of the resonator, m is the azimuthal mode number, and $n_{eff}(\lambda_m)$ is an effective index of refraction related to the mode's propagation constant $\beta(\omega)$ via $\beta(\omega) = n_{eff}(\omega)\omega/c$ (see e.g. Refs. [8, 9]). The free-spectral range f_{FSR} of a resonator is the *local* frequency spacing between modes,

calculated via:

$$f_{FSR} \approx \nu_{m+1} - \nu_m \approx \nu_m - \nu_{m-1}, \quad (1.1)$$

$$= \frac{\partial \nu_m}{\partial m}, \quad (1.2)$$

$$= \frac{c}{n_{eff}(\nu)L} - \frac{mc}{n_{eff}^2(\nu)L} \frac{\partial n_{eff}}{\partial \nu} \frac{\partial \nu}{\partial m}, \quad (1.3)$$

so that, rearranging, we obtain:

$$f_{FSR} = \frac{c/L}{\left(n_{eff} + \nu \frac{\partial n_{eff}}{\partial \nu}\right)} = \frac{c}{n_g L} = 1/T_{RT}, \quad (1.4)$$

where $n_g = n_{eff} + \nu \frac{\partial n_{eff}}{\partial \nu}$ is the group velocity of the mode and T_{RT} is the mode's round-trip time. The effective index n_{eff} is frequency dependent due to both intrinsic material dispersion and geometric dispersion, where the latter results for example from different sampling of core versus cladding material properties for different wavelength-dependent mode areas. A frequency-dependent n_{eff} leads to a frequency dependence of n_g and f_{FSR} , and a resulting non-uniform spacing in the cavity modes in frequency despite the linearity of ν_m in m .

Depending on the design, microring resonators can support a single propagating transverse mode profile or may be multi-mode, meaning that many different transverse mode profiles are supported. The former can be readily achieved using chip-integrated photonic waveguides that provide index contrast and transverse confinement on four sides; the latter is typical of resonators that lack an inner radius dimension and therefore exhibit less spatial confinement, such as free-standing silica microrod resonators [10]. For a given resonator geometry, to calculate the frequency-dependent effective index $n_{eff}(\nu)$, thereby enabling calculation of the resonance frequencies and wavelengths, one must solve Maxwell's equations for the resonator geometry. Except in special cases of high symmetry [11], this is typically done numerically using finite-element modeling tools like COMSOL. The modes of an optical resonator, both within a mode family defined by a transverse mode profile (such that they differ only by azimuthal mode number) and between mode families, must be orthogonal [12], meaning that there is no linear coupling between them.

1.1.1 Resonant enhancement in a microring resonator

The lifetime τ_γ of circulating photons in a resonator is fundamental to its fitness for applications. Generally, two processes lead to the loss of circulating photons: intrinsic dissipation that occurs at a rate $1/\tau_{int}$ and out-coupling to an external waveguide that occurs at a rate $1/\tau_{ext}$, leading to a total loss rate of $\tau_\gamma^{-1} = \tau_{ext}^{-1} + \tau_{int}^{-1}$. To understand the quantitative role of these parameters, we consider a cavity mode of frequency ω_0 and amplitude a (normalized such that $|a|^2 = N$, the number of circulating photons) driven by a pump field with frequency ω_p and rotating amplitude $s \propto \exp(i\omega_p t)$ (normalized such that $|s|^2 = S$, the rate at which photons in the coupling waveguide pass the coupling port) that is in-coupled with strength κ . The equation of motion for such a system is [12]:

$$\frac{da}{dt} = i\omega_0 a - \left(\frac{1}{2\tau_{int}} + \frac{1}{2\tau_{ext}} \right) a + \kappa s. \quad (1.5)$$

We can immediately solve this equation by assuming that $a \propto \exp(i\omega_p t)$, and we obtain:

$$a = \frac{\kappa S}{\left(\frac{1}{2\tau_{int}} + \frac{1}{2\tau_{ext}} \right) + i(\omega_p - \omega_0)}. \quad (1.6)$$

check this
and all the
math here

The time-reversal symmetry that is inherent in this system when there is no dissipation, i.e. when $1/\tau_{int} = 0$, can be exploited to show that $|\kappa|^2 = 1/\tau_{ext}$ [12]. By squaring Eq. 1.6 and inserting this expression, we find:

$$N = \frac{\Delta\omega_{ext} S}{\Delta\omega_{tot}^2/4 + (\omega_p - \omega_0)^2}, \quad (1.7)$$

where we have defined the rates $\Delta\omega_{ext} = 1/\tau_{ext}$, $\Delta\omega_{int} = 1/\tau_{int}$, and $\Delta\omega_{tot} = \Delta\omega_{ext} + \Delta\omega_{int}$. Two important observations can be drawn from Eq. 1.7: First, the cavity response is Lorentzian with a full-width at half-maximum (FWHM) linewidth that is related to the photon lifetime via $\tau_\gamma = 1/\Delta\omega_{tot}$, and second, on resonance the number of circulating photons is related to the input rate by the factor $\Delta\omega_{ext}/\Delta\omega_{tot}^2$. The combination of this resonant enhancement and a small cavity mode volume enables very large circulating optical intensities, which is important for the application of microresonators in nonlinear optics.

Two commonly used practical quantities are linked to the photon lifetime: the resonator finesse $\mathcal{F} = 2\pi\tau_\gamma/T_{RT}$, which for a ring resonator can be interpreted literally as the azimuthal resonator

angle traced out by a typical photon over its lifetime; and the resonator quality factor $Q = \omega_c \tau_\gamma$, the phase over which the optical field evolves during the photon lifetime. Using the relationship $\tau_\gamma = 1/\Delta\omega_{tot}$, the finesse and quality factor can be rewritten as simple ratios of the relevant frequencies: $\mathcal{F} = f_{FSR}/\Delta\nu$; $Q = \nu_c/\Delta\nu$, where $\Delta\nu = \Delta\omega_{tot}/2\pi$.

1.1.2 Thermal effects in microresonators

In a typical microresonator frequency-comb experiment, a frequency-tunable pump laser is coupled evanescently into and out of the resonator using a tapered optical fiber [13] (for e.g. free-standing silica disc resonators) or a bus waveguide (for chip-integrated resonators, e.g. in silicon nitride rings). When spatial overlap between the evanescent mode of the coupler and a whispering-gallery mode of the resonator is achieved, with the frequency of the pump laser close to the resonant frequency of that mode, light will build up in the resonator and the transmission of the pump laser past the resonator will decrease.

In any experiment in which a significant amount of pump light is coupled into a resonator, one immediately observes that the cavity resonance lineshape in a scan of the pump-laser frequency is not Lorentzian as expected from Eq. 1.7; plots of measured resonance lineshapes are shown in Fig. 1.2a. This is due to heating of the resonator as it absorbs circulating optical power. Since the volume of a pumped mode and the physical volume of the microresonator are both small, thermal effects have significant practical implications in microresonator experiments. As the volume of the mode heats (over a ‘fast thermal timescale’) and this energy is conducted to and heats the rest of the resonator (over the ‘slow thermal timescale’) [14], the resonance frequency of a given cavity mode shifts due to the thermo-optic coefficient $\partial n/\partial T$ and the coefficient of thermal expansion of the mode volume $\partial V/\partial T$. For typical microresonator materials the thermo-optic effect dominates, and $\partial n/\partial T > 0$ leads to a decrease in the resonance frequency with increased circulating power in steady state.

A calculation of the thermal dynamics of the system [15] composed of the pump laser and the resonator reveals that there is a range of pump-laser frequencies ω_p (which depends on the pump

laser power) near and below the ‘cold-cavity’ resonance frequency of a given cavity mode over which the system has three possible thermally-shifted resonance frequencies $\omega_{0,shifted}$ at which thermal steady state is achieved. Generally, these points are:

- (1) $\omega_p > \omega_{0,shifted}$, blue detuning with significant coupled power and thermal shift
- (2) $\omega_p < \omega_{0,shifted}$, red detuning with significant coupled power and thermal shift
- (3) $\omega_p \ll \omega_0$, red detuning with insignificant coupled power and insignificant thermal shift

These points are depicted schematically in Fig. 1.2b. Steady-state point (1) is experimentally important, because in the presence of pump-laser frequency and power fluctuations it leads to so-called thermal ‘self-locking.’ Specifically for steady-state point (1), this can be seen as follows:

- If the pump-laser power increases the cavity heats, the resonance frequency decreases, the detuning increases, and the change in coupled power is minimized.
- If the pump-laser power decreases the cavity cools, the resonance frequency increases, the detuning decreases, and the change in coupled power is minimized.
- If the pump-laser frequency increases the cavity cools, the resonance frequency increases, and the change in coupled power is minimized.
- If the pump-laser frequency decreases the cavity heats, the resonance frequency decreases, and the change in coupled power is minimized.

This is in contrast with steady-state point (2), where each of the four pump-laser fluctuations considered above generates a positive feedback loop, with the result that any fluctuation will push the system towards point (1) or point (3). This preference of the system to occupy point (1) or point (3) over a range of pump-laser detuning is referred to as thermal bistability. One consequence of this bistability is that the transmission profile of the pump laser takes on hysteretic behavior in a scan over a cavity resonance with significant pump power: in a decreasing frequency scan, the lineshape takes on a broad sawtooth shape, while in an increasing frequency scan, the resonance

takes on a narrow pseudo-Lorentzian profile whose exact shape depends on the scan parameters relative to the thermal timescale. A second consequence is that operation at red detuning with significant coupled power in a microresonator experiment requires special efforts to mitigate the effects of thermal instability.

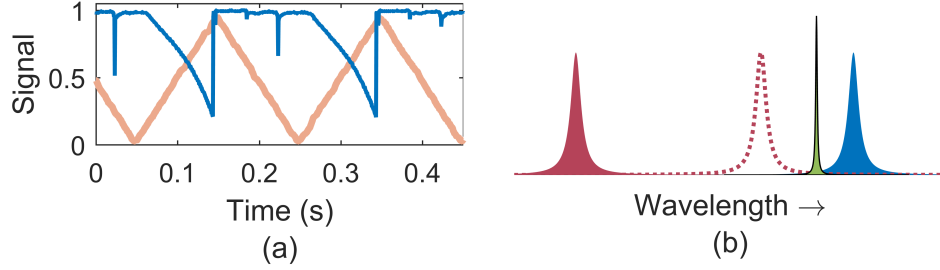


Figure 1.2: **Thermal bistability in microresonators.** (a) Measurement of power transmitted past the microresonator in an experiment using a ~ 16.5 GHz-FSR microdisk resonator and a tapered fiber. The laser wavelength is adjusted by an intracavity piezo-electric crystal. Here, larger control signal (orange) corresponds to longer laser wavelength. As the laser wavelength is increased, the resonator heats and a sawtooth-shaped resonance is observed. As the resonator wavelength is decreased, the system will ‘flip’ from steady-state point (3) to steady-state point (1), leading to observation of a narrow pseudo-Lorentzian resonance, with the exact shape depending on the thermal and scanning timescales. (b) Depiction of the three steady-state points for the laser detuning. For fixed laser wavelength (green), stable steady-state points exist with relatively small blue detuning and significant coupled power (solid blue), and relatively large red detuning and little coupled power (solid red). An unstable steady-state point also exists with red detuning and significant coupled power (dashed red). Note in this terminology that the color of the detuning (red or blue) refers to the position of the laser relative to the position of the resonance in wavelength space.

1.2 Microring resonator Kerr frequency combs

The high circulating optical intensities accessible in resonators with long photon lifetimes find immediate application in the use of microresonators for nonlinear optics. The experiments described in this thesis are conducted in silica microresonators. Silica falls into a broader class of materials that exhibit both centro-symmetry, which dictates that the second-order nonlinear susceptibility $\chi^{(2)}$ must vanish, and a significant third-order susceptibility $\chi^{(3)}$. The n^{th} -order susceptibility is a term in the Taylor expansion describing the response of the medium’s polarization to an external electric field [16]: $P = P_0 + \epsilon_0 \chi^{(1)} E + \epsilon_0 \chi^{(2)} E^2 + \epsilon_0 \chi^{(3)} E^3 + \dots$. The effect of $\chi^{(3)}$ can be described

in a straightforward way as a dependence of the refractive index on the local intensity [8],

$$n = n_0 + n_2 I \quad (1.8)$$

where $n_2 = \frac{3\chi^{(3)}}{4n_0^2\epsilon_0 c}$ [8, 17]. The intensity-dependence of the refractive index resulting from the third-order susceptibility $\chi^{(3)}$ is referred to as the optical Kerr effect.

The combination of the Kerr effect and the high circulating intensities that are accessible in high-finesse cavities provides a powerful platform for nonlinear optics. Specifically, the Kerr effect enables self-phase modulation, cross-phase modulation, and four-wave mixing, the last of which is depicted schematically in Fig. 1.3.

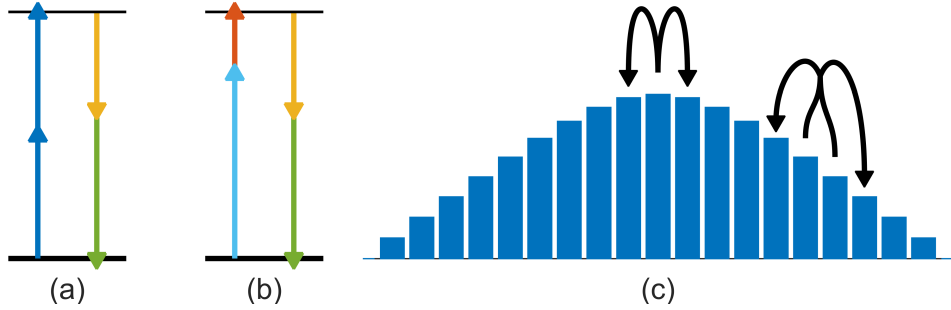


Figure 1.3: **An illustration of four-wave mixing and frequency-comb generation.** (a) Degenerate four-wave mixing, in which two fields of the same frequency ω_1 (blue) mix and generate fields at two new frequencies ω' and ω'' (yellow and green). The schematic indicates the energy-conservation requirements of the process, which can be written down as $2\omega_1 = \omega' + \omega''$. (b) Non-degenerate four-wave mixing, in which two fields of different frequencies ω_2 and ω_3 (light blue and orange) mix to generate fields at frequencies ω' and ω'' (yellow and green). Energy conservation is now expressed at $\omega_2 + \omega_3 = \omega' + \omega''$. (c) Schematic demonstration of one degenerate FWM step and one non-degenerate FWM step in a cascaded four-wave mixing process that generates a frequency comb. Figure after Ref. [1].

In 2007, a remarkable result brought the beginning of a new era for frequency comb research. Del’Haye et al. reported *cascaded four-wave mixing* (CFWM, shown in Fig. 1.3c) in toroidal silica microcavities on silicon chips, the result of which was a set of many co-circulating optical fields that were uniformly spaced by f_{rep} ranging from 375 GHz to ~ 750 GHz (depending on the platform) [18]. Measurements indicated that the frequency spacing was uniform to a precision of 7.3×10^{-18} , thereby establishing that the output of the system was a frequency comb. This result built on previous demonstrations of few-mode parametric oscillations in microresonators [19–21], and showed that the non-uniform distribution of cavity resonance frequencies due to dispersion could be overcome to

generate an output with equidistant frequency modes. A second important development occurred in 2012, when Herr et al. reported the generation of frequency combs corresponding in the time domain to single circulating optical ‘soliton’ pulses [Herr2014wArxiv]. This observation followed the observation of solitons in formally-equivalent passive fiber-ring resonators in 2010 [22]. Due to unique properties that make them particularly well-suited for applications, as discussed in Sec. 1.6, the generation and manipulation of soliton combs has become a significant priority in microcomb research.

1.3 A model for Kerr-comb nonlinear optics: The Lugiato-Lefever equation

Kerr-comb generation can be motivated and partially understood through the CFWM picture [23], but the phase and amplitude degrees of freedom for each comb line mean that CFWM gives rise to a rich space of comb phenomena—it is now known that Kerr combs can exhibit several fundamentally distinct outputs. A useful model for understanding this rich space is the Lugiato-Lefever equation (LLE), which was shown to describe microcomb dynamics by Chembo and Menyuk [24] through Fourier-transformation of a set of coupled-mode equations describing CFWM and by Coen, Randle, Sylvestre, and Erkintalo [25] through time-averaging of an Ikeda map for a low-loss resonator (as first performed by Haelterman, Trillo, and Wabnitz [26]). The LLE is a nonlinear partial-differential equation that describes evolution of the normalized cavity field envelope ψ over a slow time $\tau = t/2\tau_\gamma$ in a frame parametrized by the ring’s azimuthal angle θ (running from $-\pi$ to π) co-moving at the group velocity. The equation as formulated by Chembo and Menyuk, as it will be used throughout this thesis, reads:

$$\frac{\partial \psi}{\partial \tau} = -(1 + i\alpha)\psi + i|\psi|^2\psi - i\frac{\beta}{2}\frac{\partial^2 \psi}{\partial \theta^2} + F. \quad (1.9)$$

This equation describes ψ over the domain $-\pi \leq \theta \leq +\pi$ with periodic boundary conditions $\psi(-\pi, \tau) = \psi(\pi, \tau)$. Here F is the strength of the pump laser, with F and ψ both normalized so that they take the value 1 at the absolute threshold for parametric oscillation: $F = \sqrt{\frac{8g_0\Delta\omega_{ext}}{\Delta\omega_{tot}^3} \frac{P_{in}}{\hbar\omega_p}}$,

$|\psi|^2 = \frac{2g_0 T_{RT}}{\hbar \omega_p \Delta \omega_{tot}} P_{circ}(\theta, \tau)$, so that $|\psi(\theta, \tau)|^2$ is the instantaneous normalized power at the co-moving azimuthal angle θ . Here $g_0 = n_2 c \hbar \omega_p^2 / n_g^2 V_0$ is a parameter describing the four-wave mixing gain, $\Delta \omega_{ext}$ is the rate of coupling at the input/output port, $\Delta \omega_{tot} = 1/\tau_\gamma$ is the FWHM resonance linewidth, P_{in} is the pump-laser power, $P_{circ}(\theta, \tau)$ is the local circulating power in the cavity, \hbar is Planck's constant, and ω_p is the pump-laser frequency. The parameters n_2 , n_g , and V_0 describe the nonlinear (Kerr) index (see Eqn. 1.8), the group index of the mode, and the effective nonlinear mode volume at the pump frequency; L is the physical round-trip length of the ring cavity.

The parameters α and β describe the normalized frequency detuning of the pump laser and second-order dispersion of the resonator mode family into which the pump laser is coupled: $\alpha = -\frac{2(\omega_p - \omega_0)}{\Delta \omega_{tot}}$, $\beta = -\frac{2D_2}{\Delta \omega_{tot}}$; here $D_2 = \left. \frac{\partial^2 \omega_\mu}{\partial \mu^2} \right|_{\mu=0}$ is the second-order modal dispersion parameter, where μ is the pump-referenced mode number of Eq. ???. The parameters $D_1 = \left. \frac{\partial \omega_\mu}{\partial \mu} \right|_{\mu=0} = 2\pi f_{FSR}$ and D_2 are related to the derivatives of the propagation constant $\beta_{prop} = n_{eff}(\omega)\omega/c$ via $D_1 = 2\pi/L\beta_1$ and $D_2 = -\frac{D_1^2}{\beta_{prop,1}}\beta_{prop,2}$, where $\beta_{prop,n} = \partial^n \beta_{prop} / \partial \omega^n$. The subscript *prop* is used here to distinguish the propagation constant from the LLE dispersion coefficients $\beta_n = -2D_n/\Delta \omega_{tot}$, as unfortunately the use of the symbol β for both of these quantities is standard. Expressions for higher-order modal dispersion parameters D_n in terms of the expansion of the propagation constant can be obtained by evaluating the equation $D_n = (D_1 \frac{\partial}{\partial \mu})^n \omega_\mu$. check

The formulation of the LLE in terms of dimensionless normalized parameters helps to elucidate the fundamental properties of the system and facilitates comparison of results obtained in platforms with widely different experimental conditions. In words, the LLE relates the time-evolution of the intracavity field (normalized to its threshold value for cascaded four-wave mixing) to the power of the pump laser (normalized to its value at the threshold for cascaded four-wave mixing), the pump-laser detuning (normalized to half the cavity linewidth), and the cavity second-order dispersion quantified by the change in the FSR per mode (normalized to half the cavity linewidth). One example of the utility of this formulation is that it makes apparent the significance of the cavity linewidth in determining the output comb, and underscores the fact that optimization of the dispersion, for example, without paying heed to the effect of this optimization on the cavity linewidth, may not

yield the desired results.

The LLE is, of course, a simplified description of the dynamics occurring in the microresonator. It abstracts the nonlinear dynamics and generally successfully describes the various outputs that can be generated in a microresonator frequency comb experiment. The LLE is a good description of these nonlinear dynamics when the resonator photon lifetime, mode overlap, and nonlinear index n_2 are roughly constant over the bandwidth of the generated comb, and when the dominant contribution to nonlinear dynamics is simply the self-phase modulation term $i|\psi|^2\psi$ arising from the Kerr nonlinearity. The LLE neglects polarization effects, thermal effects, and the Raman scattering and self-steepening nonlinearities, although in principle each of these can be included [8, 27–29]. It is also worth emphasizing that the LLE can be derived from a more formally-accurate Ikeda map (as is done by Coen et al. [25]), in which the effect of localized input- and output-coupling is included in the model. This is achieved by ‘delocalizing’ the pump field and the output-coupling over the round trip, including only their averaged effects. This is an approximation that is valid in the limit of high finesse due to the fact that the cavity field cannot change on the timescale of a single round trip, but as a result the LLE necessarily neglects all dynamics that might have some periodicity at the round-trip time; the fundamental timescale of LLE dynamics is the photon lifetime.

The LLE provides a useful framework for the prediction and interpretation of experimental results. Basically, it predicts the existence of two fundamentally distinct types of Kerr-combs: extended temporal patterns and localized soliton pulses. These predictions are born out by experiments, the interpretation of which is facilitated by insight gained from the LLE. In the remainder of this chapter I briefly present some simple analytical results that can be obtained from the LLE, and then discuss these two types of comb outputs. This discussion provides context for the results presented in the next two chapters. Fig. 1.4 summarizes the results that will be presented in the remainder of this chapter, and in particular shows the values of the parameters α and F^2 at which solitons and extended patterns can be obtained.

verify that
I can see
chaos out-
side of
threshold

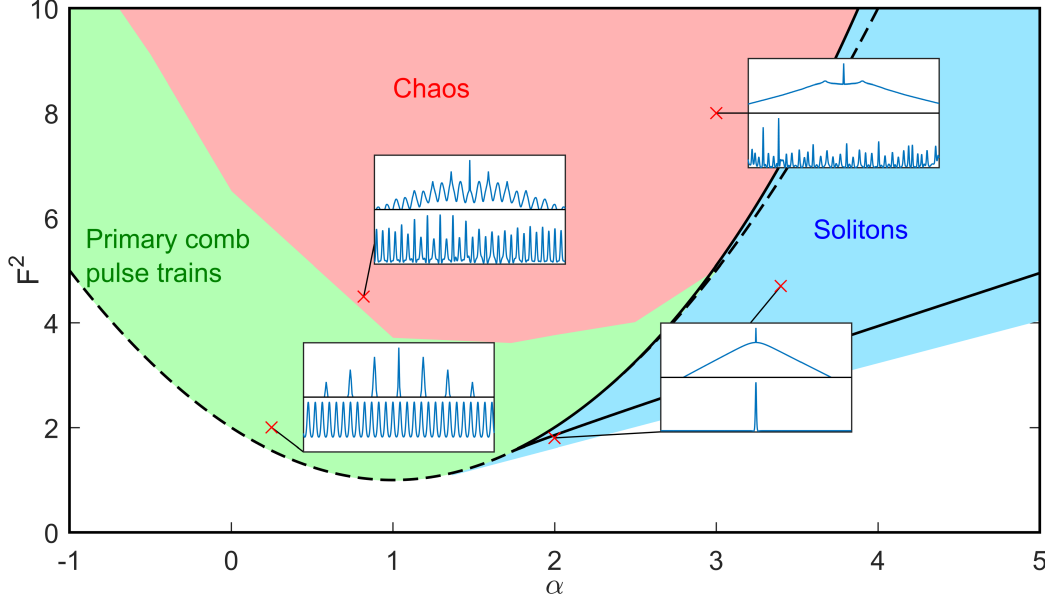


Figure 1.4: **Solution space for the Lugiato-Lefever equation.** Depiction of the various behaviors exhibited by ψ as a function of its position in the $\alpha - F^2$ plane; this predicts the type of Kerr-comb output as a function of the pump-laser detuning and power, the parameters which can be most readily adjusted in experiment. Curves plotted in black are obtained through analytical investigation of the LLE; these include the threshold curve for parametric oscillation (dashed black, Eq. 1.15) and the lines obtained via $\rho(\alpha, F^2) = \rho_{\pm}(\alpha)$ (solid black, Eq. 1.13), which define the region where the LLE exhibits multiple flat ($\partial\psi/\partial\theta = 0$, Eq. 1.10) solutions. Extended patterns arise above the threshold curve through modulation instability. Solitons exist outside of the threshold curve at higher red detuning, up to an approximate maximum $\alpha_{max} = \pi^2 F^2/8$. The lines bounding the existence of chaos are not known precisely, and in fact chaos can be observed in simulation outside of the threshold curve at values $\alpha > \alpha_{thresh,+}$ (Eq. 1.16).

1.4 Analytical investigation of the resonator's CW response

Some insight into comb dynamics can be obtained via analytical investigations of the LLE, Eq. 1.9. This section largely follows the analysis of Ref. [30], with similar analysis having been performed elsewhere, for example in Refs. [25] and [31]. When the derivative term $\partial^2\psi/\partial\theta^2$ in the LLE is non-zero, ψ is necessarily broadband, and a Kerr comb has been formed. There are no known exact analytical solutions to the LLE to describe Kerr-comb outputs. However, flat solutions to the LLE ψ_s may be calculated by setting all derivatives to zero—when these solutions can be realized physically (discussed below), they describe the behavior of the CW field that exists in the resonator

in the absence of Kerr-comb formation. Upon setting the derivatives to zero, one finds:

$$F = (1 + i\alpha)\psi_s - i|\psi_s|^2\psi_s. \quad (1.10)$$

The circulating intensity $\rho = |\psi_s|^2$ is obtained by taking the modulus-square of Eq. 1.10 to obtain:

$$F^2 = (1 + (\alpha - \rho)^2) \rho, \quad (1.11)$$

$$= \rho^3 - 2\alpha\rho^2 + (\alpha^2 + 1)\rho, \quad (1.12)$$

whereupon this equation can be numerically solved for ρ . As a third-order polynomial in ρ , this equation has three solutions; complex solutions are unphysical. With α held constant, the function $F_\alpha^2(\rho)$ defined by this equation uniquely determines F^2 for a given value of ρ . By noting that $F^2(\rho = 0) = 0$ and $\partial F^2/\partial \rho|_{\rho=0} > 0$, one can conclude that three real solutions for the inverted function $\rho_\alpha(F^2)$ exist between the values ρ_\pm that extremize $F_\alpha^2(\rho)$:

$$\rho_\pm = \frac{2\alpha \pm \sqrt{\alpha^2 - 3}}{3}, \quad (1.13)$$

while outside of this interval there is only one real solution ρ . This is illustrated in Fig. 1.5.

Physically, the coexistence of multiple flat solutions ρ at a given point (α, F^2) corresponds to a ‘tilting’ of the Lorentzian transmission profile of the cavity and leads to bistability, even before taking into account thermal effects. This is illustrated in Fig. 1.5. Generally speaking, extended patterns exist on the upper branch of this curve, highlighted in blue, and solitons exist on the lower branch, highlighted in red. For flat solutions ρ , an effective Kerr-shifted detuning can be defined as $\alpha_{eff} = \alpha - \rho$. The discussion of thermal effects in Sec. 1.1.2 then applies to the effective detuning α_{eff} ; that is, operating with significant coupled power at *effective* red detuning is thermally unstable, while thermal locking occurs with significant coupled power at effective blue detuning. The effective detuning simply incorporates the Kerr nonlinearity into the round-trip phase shift that describes the constructive or destructive interference of the circulating field with the pump at the coupling port. By noting that $\alpha = F^2 = \rho$ solves Eq. 1.11, we can conclude that the position of the effective Kerr-shifted resonance is on the line $\alpha = F^2$, where $\alpha_{eff} = 0$. For fixed F^2 , an effectively red-detuned

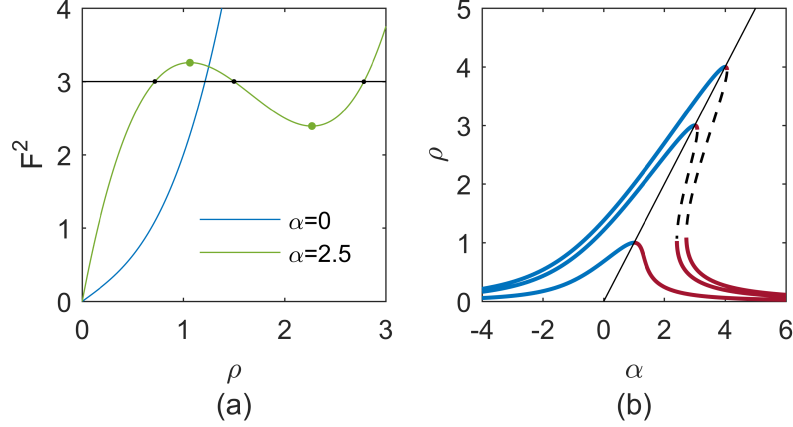


Figure 1.5: **Investigation of the circulating CW power in a Kerr resonator.** (a) Plots of F^2 as a function of ρ for $\alpha = 0$ (blue) and $\alpha = 2.5$ (green), according to Eq. 1.11. When values of ρ exist that extremize F^2 according to this equation, multiple real solutions for the circulating power ρ (shown as black dots in this example) exist between these extremal values of F^2 (shown as green dots in this example). (b) Kerr-tilted resonances curves $\rho(\alpha)$ for $F^2 = 1$ (smallest), 3 , and 4 (largest). The line $\rho = \alpha = F^2$ (solid black) marks the highest circulating power for a given input power F^2 and separates the effectively blue-detuned and effectively red-detuned branches. When $F^2 > 8\sqrt{3}/9$ (obtained by solving for $\rho_+ = \rho_-$, Eq. 1.13), the resonance becomes tilted steeply enough that an unstable middle branch (dashed black) exists.

branch of the tilted resonance exists above the value of α where ρ becomes multivalued. This value of α can be determined by inserting ρ_- (Eq. 1.13) into Eq. 1.11 and solving for α .

Once the circulating intensity ρ is known, the corresponding flat solution ψ_s can be determined from Eq. 1.10 by inserting the known value of ρ and solving for ψ_s , with the result:

$$\psi_s = \frac{F}{1 + i(\alpha - \rho)}. \quad (1.14)$$

This expression reveals that the flat solution acquires a phase $\phi_{CW} = \tan^{-1}(\rho - \alpha)$ relative to the pump.

If the flat solution(s) at a point (α, F^2) is (are) unstable, a Kerr comb will form spontaneously. Stability analysis of the flat solutions can be performed, and the results are [30]:

- In the region of multi-stability, if the flat solutions are ordered with increasing magnitude as ρ_1 , ρ_2 , and ρ_3 , the middle solution ρ_2 is always unstable.
- A flat solution ρ that is not the middle solution is stable if $\rho < 1$; otherwise it is unstable.

When the flat solution is unstable, the mode that experiences the greatest instability has mode number $\mu_{max} = \sqrt{\frac{2}{\beta}(\alpha - 2\rho)}$.

Therefore, the pump-laser threshold curve for Kerr-comb generation can be determined in the $\alpha - F^2$ plane by setting $\rho = 1$ in Eq. 1.10:

$$F_{thresh}^2 = 1 + (\alpha - 1)^2, \quad (1.15)$$

$$\alpha_{thresh,\pm} = 1 \pm \sqrt{F^2 - 1}, \quad (1.16)$$

for an experiment in which the pump power or detuning is tuned while the other is held fixed.

1.5 Kerr comb outputs: extended modulation-instability patterns

Extended temporal patterns arise spontaneously as a result of the instability of the flat solution to the LLE when the pump laser is tuned above the threshold curve. These patterns can be stationary, in which case they are typically referred to as ‘Turing patterns’ or ‘primary comb,’ or can evolve in time, in which case they are typically referred to as ‘noisy comb’ or ‘spatiotemporal chaos.’ In general, the former occurs for lower values of the detuning α and smaller pump strengths F^2 ; although some studies of the transition from Turing patterns to chaos have been conducted [others, 32], a well-defined boundary between the two has not been established, and may not exist.

In the spatial domain parametrized by θ , a Turing pattern consists of a pulse train with (typically) $n \gg 1$ pulses in the domain $-\pi \leq \theta \leq \pi$ —the pulse train’s repetition rate is a multiple of the cavity FSR: $f_{rep} = n \times f_{FSR}$. Corresponding to the n -fold decreased period (relative to the round-trip time) of an n -pulse Turing pattern’s modulated waveform in the time domain, the optical spectrum of a Turing pattern consists of modes spaced by n resonator FSR—it is this widely-spaced spectrum that is referred to as ‘primary comb.’ Analytical approximations for Turing patterns are possible near threshold [33, 34] and in the small damping limit [35]. The stability analysis results from the last section can be used to predict the spacing n of a primary comb (equivalently the number of Turing-pattern pulses) generated in a decreasing-frequency scan across the resonance with fixed normalized pump power F^2 : $n = \mu_{max,thresh} = \sqrt{\Delta\omega_0(1 + \sqrt{F^2 - 1})/D_2}$.

Spatiotemporal chaos can be understood as a Turing pattern whose pulses oscillate in height, with adjacent pulses oscillating out of phase. From such an oscillating Turing pattern, if α and/or F^2 is increased, one moves deeper into the chaotic regime and pulses begin to exhibit lateral motion and collisions; the number of pulses present in the cavity is no longer constant in time. Depending on the severity of the chaos (higher for larger α and F^2), a chaotic comb may correspond to a primary-comb-type spectrum with each primary-comb mode exhibiting sidebands at the resonator FSR, so-called ‘subcombs,’ or it may correspond to a densely-populated spectrum with light in each cavity mode.

Relative to generation of solitons, experimental generation of an extended pattern is straightforward. As shown in Fig. ??, these patterns are generated with blue effective pump-laser detuning $\alpha_{eff} < 0$, where thermal locking occurs. Because they arise spontaneously from noise, their generation is (comparatively) straightforward: simply decrease the pump-laser frequency until a pattern is generated. Unfortunately, operation of a Kerr-comb in the extended pattern regime is disadvantageous for applications: the n -FSR spacing of primary comb presents a challenge for measurement of the repetition rate of the frequency comb due to the bandwidth of measurement electronics, and the aperiodic time-evolution of chaotic comb corresponds to modulation sidebands on the comb modes within the linewidth of the cavity that preclude the use of the comb as a set of stable optical reference frequencies.

An important property of these extended patterns is that they fill the resonator—the characteristic size of temporal features scales roughly as $1/\sqrt{-\beta}$, but these features are distributed densely and uniformly throughout the resonator. This means that the total circulating power of an extended pattern $\int d\theta |\psi|^2$ is large relative to the localized pulses discussed in the next section, and therefore that extended patterns come with a comparatively large thermal shift of the resonance.

1.6 Kerr comb outputs: solitons

The term ‘soliton’ generally refers to a localized excitation that can propagate without changing its shape due to a delicate balance between dispersion (or diffraction) and nonlinearity. Solitons are

found in several contexts within the field of nonlinear optics, and temporal Kerr-soliton pulses in optical fibers are particularly well known. Microresonators support so-called dissipative cavity solitons, which are localized pulses circulating the resonator that are out-coupled once per round trip. In the case of a single circulating soliton, this leads to a train of pulses propagating away from the resonator with repetition rate $1/T_{RT}$. Thus the mode spacing of the comb matches the FSR of the resonator, in contrast with widely-spaced primary comb spectra, and the soliton can, in principle, propagate indefinitely as a stationary solution to the LLE. This makes Kerr combs based on solitons particularly attractive for applications.

Solitons in optical fibers are solutions of the nonlinear Schrodinger equation (NLSE) that describes pulse-propagation in optical fiber [8]:

$$\frac{\partial A}{\partial z} = i\gamma|A|^2A - i\frac{\beta}{2}\frac{\partial^2 A}{\partial T^2}. \quad (1.17)$$

This equation describes the evolution of the pulse envelope A in the ‘fast-time’ reference frame parametrized by T as it propagates down the length of the fiber, parametrized by the distance variable z . Here γ is the nonlinear coefficient of the fiber and $\beta_{prop,2}$ is the GVD parameter. The LLE can be viewed as an NLSE with additional loss and detuning terms $-(1+i\alpha)\psi$ and a driving term F .

The fundamental soliton solution to the NLSE is:

$$A_{sol} = \sqrt{P_0} \operatorname{sech}(T/\tau) e^{i\gamma P_0 z/2 + i\phi_0}, \quad (1.18)$$

where P_0 is the peak power of the pulse and is related to the duration of the pulse τ via $\tau = \sqrt{-\beta/\gamma P_0}$, and ϕ_0 is an arbitrary phase. Thus, this equation admits a *continuum* of pulsed fundamental ‘soliton’ solutions, with one existing for each value of the peak power. Each of these solutions propagates down the fiber without changing shape; only the phase evolves with distance as $\phi(z) = \gamma P_0 z/2 + \phi_0$.

The introduction of the loss, detuning, and driving terms into the NLSE to obtain the LLE has several important consequences for solitons. First, exact analytical expressions for the soliton solution to the LLE in terms of elementary functions are not known, in contrast with the situation

reference to
the above,
also do I
need a 2
here

for the NLSE. However, the soliton solutions to the LLE, Eq. 1.9, can be approximated well as:

$$\psi_{sol} = \psi_{s,min} + e^{i\phi_0} \sqrt{2\alpha} \operatorname{sech} \sqrt{\frac{2\alpha}{-\beta}} \theta. \quad (1.19)$$

Here $\psi_{s,min}$ is the flat solution to the LLE from Eq. 1.14 at the point where the soliton solution is desired; when multiple flat solutions exist, $\psi_{s,min}$ is the one corresponding to the smallest intensity ρ_1 . The phase $\phi_0 = \cos^{-1}(\sqrt{8\alpha}/\pi F)$ arises from the intensity-dependent phase shift in the cavity due to the Kerr effect, mathematically described by the term $i|\psi|^2\psi$.

This approximation ψ_{sol} from Eq. 1.19 for the soliton solution of the LLE illustrates a second important consequence of the differences between the NLSE and the LLE: while the NLSE admits a continuum of fundamental soliton solutions parametrized by their peak power P_0 and arbitrary phase ϕ_0 , the LLE supports only one shape for the envelope of a soliton for fixed experimental parameters α and F^2 . Intuitively, this can be understood as arising from the need for a balance between dispersion and nonlinearity, as in the NLSE, *and* between loss (described by $\partial\psi/\partial\tau = -\psi + \dots$) and the pump (described by $\partial\psi/\partial\tau = \dots + F$) for stable evolution of an LLE soliton—the driving term is not scaled by ψ , which instead would represent linear gain, and therefore provides an absolute reference that fixes the amplitude of the soliton.

The amplitude of the LLE soliton depends only on the detuning α , and the width of the soliton increases with larger detuning α and smaller dispersion β . These characteristics are apparent from the analytical approximation in Eq. ??, but are also evident in numerical calculations of the exact soliton solution to the LLE [36].

Solitons exist only where there is a flat solution ψ_s that is effectively red detuned that can form the background for the pulse [31, 37]. Consistent with the phase ϕ_0 in the approximation ψ_{sol} in Eq. 1.19, solitons can exist up to a maximum detuning of $\alpha_{max} = \pi^2 F^2 / 8$ [28].

Solitons are strongly localized: the deviation of the background intensity from ρ_1 near a soliton at θ_0 is proportional to $e^{-(\theta-\theta_0)/\delta\theta}$, where $\delta\theta = \sqrt{-\beta/2\alpha}$. If $\delta\theta$ is sufficiently small, multiple solitons can be supported in the resonator domain $-\pi \leq \theta \leq \pi$ with negligible interactions between solitons. Simulations reveal that if $(\theta - \theta_0)/\delta\theta$ is too small, solitons exhibit attractive interactions; the result

check if this
is an ap-
propriate
reference

should I add
some refer-
ences here?

of this attraction can be pair-wise annihilation or pair-wise merger, with the ultimate result being a stable soliton ensemble with fewer solitons. The maximum number of solitons that can coexist in a resonator in the absence of higher-order stabilizing effects (see Chapter ??) can be approximated as $N_{max} \approx \sqrt{-2/\beta}$ [28]. An approximation to the form of a soliton ensemble is possible as:

$$\psi_{ens} = \psi_{s,min} + e^{i\phi_0} \sqrt{2\alpha} \sum_j \text{sech} \left(\sqrt{\frac{2\alpha}{-\beta}} (\theta - \theta_j) \right), \quad (1.20)$$

where $\{\theta_j\}$ define the positions of the solitons in the ensemble and $\phi_0 = \cos^{-1}(\sqrt{8\alpha}/\pi F)$ as above.

The spectrum of a single-soliton Kerr comb has a $\text{sech}^2(\Omega/\Delta\Omega)$ envelope, where Ω is the optical angular frequency and $\Delta\Omega \approx \sqrt{32\alpha/|\beta|T_{RT}^2}$ is the bandwidth of the pulse in angular frequency. Equivalently, the bandwidth of the soliton in (linear) optical frequency is $\sqrt{\frac{16\Delta\nu f_{rep}^2}{D_2}\alpha}$. For a soliton at the maximum detuning $\alpha_{max} = \pi^2 F^2/8$ for fixed normalized pump power F^2 , the bandwidth is then $\sqrt{\frac{\pi^2 \Delta\nu f_{rep}^2}{2D_2} F^2}$. Because solitons have single-FSR spacing, have the output localized into a high peak-power pulse, and are stationary (in contrast with chaos, which has single-FSR spacing but is not-stationary), they are useful for applications. Many of the proposals for and demonstrations of applications with Kerr-combs have used single-soliton operation.

1.6.1 Experimental generation of solitons

Relative to the generation of extended modulation-instability patterns, experimental generation of solitons in microring resonators is challenging. Solitons are localized excitations below threshold, which means that their existence is degenerate with their absence—a resonator can host $N = 0, 1, 2, \dots$ up to N_{max} solitons for a given set of parameters α and F^2 ; this degeneracy is illustrated in Fig. ?. If α and F^2 are experimentally tuned to a point at which solitons may exist, ψ will evolve to a form determined by the initial conditions of the field ψ . To provide appropriate initial conditions, most experimental demonstrations of soliton generation have involved first generating an extended pattern in the resonator, and then tuning to an appropriate point (α, F^2) so that ‘condensation’ of solitons from the extended pattern occurs.

Condensation of solitons from an extended pattern presents additional challenges. First, it is

difficult to control the number of solitons that emerge, due to the high degree of soliton-number degeneracy. This typically leads to a success rate somewhat lower than 100 % in the generation of single solitons. Second, the transition from a high duty-cycle extended pattern to a lower duty-cycle ensemble of one or several solitons comes with a dramatic drop in intracavity power that occurs on the timescale of the photon lifetime. If the resonator is in thermal steady-state before this drop occurs, the resonator will cool and the resonance frequency will increase. If this increase is large enough that the final detuning α exceeds $\alpha_{max} = \pi^2 F^2 / 8$, the soliton is lost. This challenge can be addressed by preparing initial conditions for soliton generation and then tuning to an appropriate point (α, F^2) before the cavity can come into thermal steady-state at the temperature determined by the larger power of the extended pattern; this is possible because the timescale over which an extended pattern can be generated is related to the photon lifetime, which is typically much faster than the thermal timescale.

The first report of soliton generation in microresonators came in a paper by Herr et al. published in 2014 [28]. These authors described optimizing the speed of a decreasing-frequency scan of the pump laser across the cavity resonance so that a soliton could be condensed from an extended pattern and the scan could then be halted at a laser frequency where the soliton could be maintained, with the system in thermal steady-state at the temperature determined by the circulating power of the soliton. Other approaches for dealing with the challenges described above have been developed since this first demonstration; these include fast manipulation of the pump power [36, 38], periodic modulation of the pump laser’s phase or power at f_{FSR} [5, 39], and tuning of the cavity resonance frequency using chip-integrated heaters instead of tuning the pump-laser frequency [Joshi2016, Wang2018a]. These methods continue to make use of extended patterns to provide initial conditions for soliton generation. In formally-equivalent fiber-ring resonators, direct generation of solitons without condensation from an extended pattern has been demonstrated using transient phase and/or amplitude modulation of the pump laser [40–42]. Chapter ?? of this thesis presents a new variation on these schemes that enables direct generation of solitons using only phase modulation at f_{FSR} without transient manipulation of the system parameters; this approach is based on a proposal by

Robust soliton crystals...

Taheri, Eftekhari, and Adibi [43].

A variety of applications of soliton-based Kerr frequency combs have already been demonstrated. Some of these include demonstrations of an optical clock [44], dual-comb spectroscopy [Suh2016], coherent communications [Marin-Palomo2018], and direct on-chip optical frequency synthesis [45].

Science 354,
600

Nature 546
274

something
else here

Chapter 2

Pulse Picking

This chapter presents a discussion of a technique for repetition-rate reduction of optical pulse trains. While high pulse train repetition rates are appealing for some applications, they are not always appropriate. For example, spectral resolution in spectroscopy applications is sacrificed in a comb with a large mode spacing, and a high repetition rate makes nonlinear optics less efficient at a given average power. This can present a barrier to the generation of octave-spanning spectra for $f - 2f$ self-referencing (see Sec. ??). On the other hand, in general the size of the comb package sets the scale for the round-trip time, meaning that low-SWAP combs tend to have inherently high repetition rates. Therefore, to increase the flexibility of low-SWAP and high-repetition-rate comb systems in applications, a method for reducing the repetition rate of a pulse train will be useful.

Here I present an investigation of a method for pulse train repetition-rate reduction, or down-sampling, in which an electro-optic gate realized by an RF-driven Mach-Zehnder interferometer periodically transmits an incoming pulse at a frequency lower than the input repetition rate. The basic principle is illustrated in Fig. 2.1. Downsampling via pulse gating, also referred to as 'pulse picking' in the literature, has been used extensively in the context of high-field, phase-sensitive ultrafast optics for the generation of energetic, carrier-envelope-phase-stabilized ultrashort pulses [46, 47]. In this application, a comb with initial repetition rate in the ~ 100 MHz range that has already been self-referenced and stabilized is pulse-picked to a repetition rate on the order of 1-100 kHz. Concerns in this application center around control and preservation of the carrier-envelope phase

only needs a
final proof-
reading and
to finish ref-
erences

also ver-
ify that
all cross-
references
appear prop-
erly

in the pulse-picking and amplification process [48, 49]. In contrast, the focus here is on downsampling within the context of optical metrology with frequency combs, and we are concerned with downsampling's effect on the optical phase noise, the pulse-to-pulse energy fluctuations, and the carrier-envelope offset frequency of the comb. In particular, it is important that the downsampled pulse train is suitable for $f - 2f$ self-referencing.

Sec. 2.1 presents a proof-of-principle experiment in which a 250 MHz pulse train is downsampled to 25 MHz, and then spectrally broadened and self-referenced. A mathematical model of downsampling is presented in Sec. 2.2, and this model informs the discussion of downsampling's effect on the pulse train's noise properties presented in Sec. 2.3 and Sec. 2.4. In Sec. 2.5 I discuss some practical considerations in applications of the technique, including the effect of imperfections in the gating process such as incomplete extinction of rejected pulses.

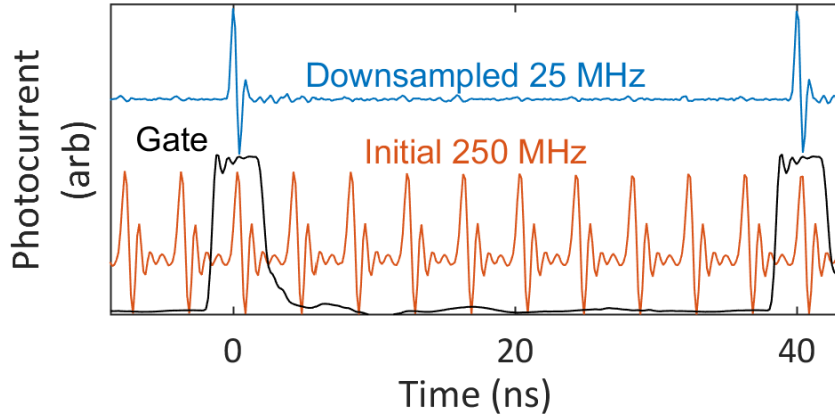


Figure 2.1: **An illustration of pulse-train repetition-rate downsampling.** Orange: A photodetected 250 MHz pulse train. Blue: A photodetected 25 MHz pulse train obtained by downsampling the 250 MHz pulse train by a factor of $N = 10$. Black: Oscilloscope trace showing the voltage sent to the RF port of a Mach-Zehnder intensity modulator to selectively transmit a subset of the incoming pulses. With the intensity modulator biased for zero transmission, the voltage trace is indicative of the transmission.

2.1 Proof-of-Concept Experiment

Here I present a proof-of-concept experiment in which a 250 MHz comb is downsampled and self-referenced. The setup for and results of this experiment are summarized in Fig. 2.2. Our pulse

gating scheme, shown in Fig. 2.2a, employs a Mach-Zehnder (MZ) electro-optic intensity modulator driven by 25 MHz rectangular electronic gating pulses with 80 ps transitions and 3.5 ns duration. The electronic pulse generator and the repetition rate of the input 250 MHz comb are both referenced to a hydrogen maser to maintain synchronization. The DC bias of the intensity modulator is set for maximum extinction outside the electronic gate, whose amplitude is approximately matched to V_π of the EOM. This downsampling scheme results in a stable 25 MHz optical pulse train with >12 dB contrast (Fig. 2.1). This contrast is adequate for this experiment, but could be improved by cascading modulators with higher extinction ratios. The average power of the 250 MHz pulse train is reduced from 30 mW to 400 μ W by the pulse gating process and the insertion loss of the optical components. The pulse train is amplified to 35 mW by use of a normal-dispersion erbium-doped fiber amplifier, which provides some spectral broadening and temporal pulse compression [50]. An octave-spanning supercontinuum is obtained by launching the amplified, <100 fs, \sim 1 nJ pulses into 20 cm of highly nonlinear fiber (HNLF) [51]; the resulting spectrum is shown in Fig. 2.2b. For comparison, we also present the supercontinuum generated by the 250 MHz comb with the EOM set for constant maximum transmission under otherwise identical conditions. The 250 MHz comb is amplified by the same EDFA to an average power of 85 mW, corresponding to 340 pJ pulse energy, before it enters the HNLF.

To detect f_0 , the octave-spanning supercontinuum shown in Fig. 2.2b is sent into a free-space $f - 2f$ interferometer consisting of a half-wave plate and a periodically poled lithium niobate (PPLN) crystal quasi-phase-matched for second-harmonic generation at 1980 nm. The generated 990 nm light is shown in 2.2b. A 10 nm band-pass filter at 990 nm selects this second harmonic and the co-linear supercontinuum at 990 nm, which are then photodetected to observe f_0 with 30 dB signal-to-noise ratio, shown in Fig. 2.2c. Fig. 2.2d shows a 2000 s record of f_0 for the downsampled comb.

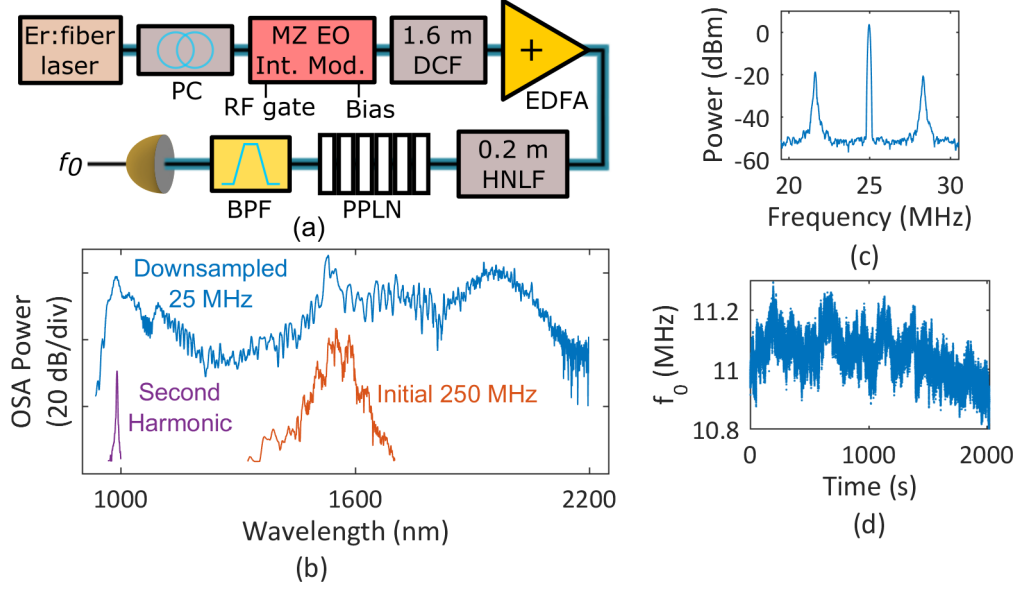


Figure 2.2: **Demonstration of downsampling for f_0 detection.** (a) Schematic depiction of the setup for downsampling a 250 MHz Er:fiber comb and detecting the offset frequency of the resulting 25 MHz pulse train. PC—polarization controller. DCF—dispersion-compensating fiber. EDFA—erbium-doped fiber amplifier. HNLF—highly nonlinear fiber. PPLN—periodically-poled lithium niobate. BPF—(optical) band-pass filter. (b) Octave-spanning supercontinuum generated by downsampling (top, blue), second harmonic generated for f_0 detection (purple), and for comparison the supercontinuum generated by the same apparatus without downsampling (orange). (c) Detected repetition rate and f_0 beat at 100 kHz resolution bandwidth; signal-to-noise ratio of f_0 is 30 dB. (d) Counted frequency of the detected free-running offset beat. Data is taken for ~ 2000 s at 10 ms gate time. The offset frequency of the 250 MHz commercial comb was adjusted between measurements shown in Figs. 2.2c and 2.2d to simplify electronic processing.

2.2 Mathematical model for downsampling

While Fig. 2.2 presents an absolute frequency measurement of f_0 enabled by downsampling, it does not demonstrate the deterministic connection between the input and downsampled combs that is essential for applications. To understand this relationship, I present first a simple model of downsampling, and then experimental tests of its conclusions.

The downsampled pulse train's electric field is modeled as the product of the incoming comb's field and a time-varying amplitude modulation. For an incoming optical frequency comb with repetition rate f_{rep} , complex single-pulse field $A(t)$ that is localized near $t = 0$, and pulse-to-pulse carrier-envelope phase shift ϕ , pulse gating by a train of rectangular pulses of length t_g and arrival

rate f_g yields a downsampled comb with field

$$a(t) = [\Sigma_n A(t - n/f_{rep})e^{in\phi}] \times [\Sigma_m \text{Rect}((t - m/f_g)/t_g)] \quad (2.1)$$

where $\text{Rect}(x)$ is the rectangle function, taking the value 1 for $-1/2 \leq x \leq 1/2$ and 0 elsewhere. Indices n and m count the pulse number of the incoming pulse train and the electronic gate respectively. The optical spectrum of the downsampled pulse train $a(t)$, calculated via the convolution theorem for the Fourier transform, is:

$$\mathcal{F}\{a\}(f) \sim 4\pi f_{rep} \Sigma_{nm} \frac{1}{m} \mathcal{F}\{A\}(f_0 + n f_{rep}) \times \sin(\pi m t_g f_g) \delta(f - f_0 - n f_{rep} - m f_g) \quad (2.2)$$

where $f_0 = f_{rep} \cdot \phi / 2\pi$ is the carrier-envelope offset frequency of the incoming comb and δ is the Dirac delta function. The downsampled pulse train has spectral content at optical modes $f_0 + n f_{rep}$, as well as at intensity modulation sidebands whose frequency offsets $m f_g$ are harmonics of the gating frequency. To avoid the generation of unwanted modulations, pulse gating at an integer sub-harmonic of the incoming repetition rate, $f_g = f_{rep}/N$, is essential. In this case superposition of the intensity modulation components created by pulse gating results in a downsampled frequency comb with a single mode spacing. Moreover, this model predicts that the offset frequency is preserved up to a reduction modulo the comb's new repetition rate.

Notably, for pulse gating at a sub-harmonic of the input comb's repetition rate, timing jitter of the electronic gate that is less than its duration does not contribute to noise on the downsampled comb. By modeling jitter as gate-to-gate arrival-time delays Δt_m , it can be shown that the downsampled comb's amplitude $a(t)$ and spectrum $\mathcal{F}\{a\}(f)$ do not deviate from Eqn. 2.1 provided that: (1) The jitter is a sufficiently small $|\Delta t_m| < t_g/2$, i.e., that the optical and electronic pulses are always substantially overlapped, and (2) That the optical pulses are substantially shorter than the electrical pulses, which is true for most systems. Thus, in general we expect that the carrier-envelope offset frequency of the incoming comb is preserved by downsampling even with jitter on the gate signal.

2.3 Experimental investigation of the effect of downsampling on the pulse train's noise properties

We supplement the mathematical model presented above with an experimental investigation of the effects of downsampling on the noise properties of the pulse train. First we consider the effects of technical limitations to ideal downsampling, and then we discuss fundamental effects associated with aliasing of high-Fourier-frequency optical noise and shot noise.

We measure the phase-noise spectrum of the downsampled comb's repetition rate at different points in our apparatus, as shown in Fig. 2.3a. We also plot the phase noise of the 250 MHz comb, which has been shifted by $-10\log_{10}(N^2) = -20$ dB to facilitate comparison [52], and the phase noise of the electronic gate. The downsampled frequency comb's phase-noise spectrum matches that of the 250 MHz comb except for a small increase at ~ 3 kHz, likely corresponding to the corner in the gate generator's phase noise at the same frequency. The phase noise of the high- and low-frequency ends of the supercontinuum similarly matches the 250 MHz comb below 1 kHz. The higher phase noise in the supercontinuum beyond 1 kHz is above the measurement system's noise floor (including shot noise), despite the reduced optical power available after spectral filtering. This higher noise is likely due to noise generation processes in the HNLF, such as the conversion of amplitude fluctuations on input pulses to timing jitter in the supercontinuum [53].

The timing jitter of our gating pulse train is between 5 ps (obtained by integrating the phase noise plotted in Fig. 2.3 to 100 kHz) and 10 ps (extrapolating constant phase noise to the 12.5 MHz Nyquist frequency and integrating). These jitter values are small relative to the 4 ns repetition period of the incoming optical pulse train. As the repetition rate of the incoming optical pulse train increases to >10 GHz, the gate duration must correspondingly decrease for single-pulse gating, and timing jitter on the gate may become a significant fraction of the gate duration. To explore the effects of timing jitter larger than our pulse generator's inherent 5 to 10 ps, we impose excess jitter on the gating signal. We modulate the relative timing between the gating signal and the incoming optical pulse train at a frequency of 5 MHz with an amplitude of 250 ps. The effect of this jitter is

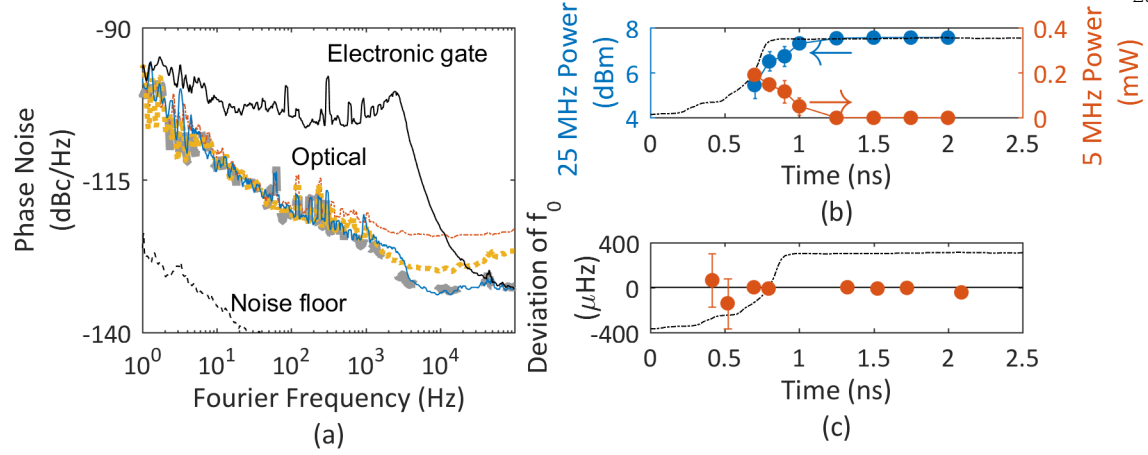


Figure 2.3: **Experimental investigation of noise introduced by downsampling.** (a) Measured repetition-rate phase noise of spectral components of the supercontinuum, selected by a 990 ± 5 nm band-pass filter (dot-dashed orange), 1650 nm long pass filter (dotted yellow), and the entire downsampled 25 MHz frequency comb measured immediately before the EDFA (solid blue), the 250 MHz comb (large-dashed gray, shifted by $20 \log(1/10) = -20$ dB). Also shown is the phase noise of the electronic gate generator (top, solid black). (b) Amplitude of the downsampled pulse-train modulation due to 250 ps jitter at 5 MHz rate. The position of a data point on the x-axis indicates its mean position within the gate, shown in dashed black. Measurement uncertainties arise due to a latency between the optical trigger and the start of the electronic gating signal which varies on the order of 50 ps. (c) Deviation of the carrier-envelope offset frequency of the downsampled comb from the 250 MHz comb's offset frequency as a function of the alignment of optical pulses within the gate.

manifest in the microwave power of the gated comb as 5 MHz intensity-modulation sidebands whose amplitude depends on the position of the optical pulses within the gate, as shown in Fig. 2.3b. Pulses with a mean position within 250 ps of the gate edge are substantially modulated by the 5 MHz gate-delay signal. This agrees with the prediction of a sharp threshold on the acceptable level of timing jitter on the gate.

It is essential to establish that the comb's carrier-envelope offset frequency is preserved in the downsampling process. To do this, we perform a frequency comparison of the 25 MHz downsampled comb and a separate output of the 250 MHz comb. This 250 MHz output is intensity modulated so that a measurement of the nonzero optical heterodyne beat frequency between an intensity modulation sideband and a pulse-gating sideband of the downsampled comb reveals the relative frequency offset of the two combs. Figure 2.3c shows the null frequency shift between the 25 MHz and 250 MHz combs, which we have characterized for different alignments of the optical pulse within the

gate. At the level of several microhertz, better than 10^{-18} relative to the 200 THz optical carrier frequency, we observe no frequency shift between the 250 MHz comb and the downsampled 25 MHz comb when the gate is properly aligned. This confirms the utility of downsampling for measurement of a high-repetition-rate comb's offset frequency for subsequent use of the comb in, for example, a spectroscopy experiment requiring high power per comb mode and high frequency precision.

2.4 Effects of ideal downsampling on a pulse train's noise properties

In addition to the conversion of electronic technical noise to optical noise on the downsampled pulse train, there exists a further mechanism by which downsampling can change the measured amplitude noise properties of the pulse train. Even ideal downsampling, free of electronic noise, leads to an increase in the measured power spectral density (PSD) of optical pulse energy fluctuations (PEF) when technical pulse energy noise is present. This is due to aliasing of components of the PSD of pulse energy fluctuations at frequencies above the Nyquist frequency of the original pulse train, $f_{rep}/2$, when the Nyquist frequency is reduced to $f_{rep}/2N$ by downsampling. Assuming random fluctuations from pulse to pulse, downsampling does not change the RMS fractional pulse energy fluctuation σ_{PEF} , whose square is equal to the frequency integral of the PSD of pulse energy fluctuations $S_{PEF}(f)$:

$$\sigma_{PEF}^2 = \int_0^{f_{rep}/2} df S_{PEF}(f). \quad (2.3)$$

—

Because the Nyquist frequency defines the upper limit for integration of S_{PEF} , in order for σ_{PEF} to be preserved $S_{PEF}(f)$ must increase when the Nyquist frequency is reduced by downsampling. For example, in the simple case of white technical noise on the pulse energies with density S_o , we have

$$\sigma_{PEF}^2 = \int_0^{f_{rep}/2} df S_o = \int_0^{f_{rep}/2N} df S' \quad (2.4)$$

which shows that downsampling must increase the measured PSD of white technical noise from

S_o to $S' = NS_o$, assuming there are no spectral correlations. However, this simple multiplicative increase is restricted to the case of white technical noise. In general, the PSD of pulse energy fluctuations of the new pulse train is determined from the original PSD through the usual method of modeling aliasing of a signal: a new Fourier frequency for each component of the original PSD is obtained by reducing the original Fourier frequency by a multiple of $-f_{rep}/N$ so that it lies between $-f_{rep}/2N$ and $f_{rep}/2N$ and taking its absolute value. The new PSD is then determined by taking the quadrature sum of the PSD components at the same aliased Fourier frequency. This phenomenon is derived mathematically and demonstrated experimentally in Ref. [48], where the analysis of carrier-envelope phase noise applies equally well to pulse energy fluctuations.

In contrast with the increase in the PSD of pulse energy fluctuations arising from coincidence of the optical pulse with the edge of the electrical gate, which increases σ_{PEF} , the aliasing mechanism described above preserves σ_{PEF} . An important consequence of this is that while technical noise can lead to supercontinuum decoherence in external nonlinear spectral broadening, aliasing does not, because it is σ_{PEF} which determines the degree of supercontinuum decoherence. Thus the aliasing mechanism impedes $f - 2f$ self-referencing only by reducing the available signal-to-noise ratio of an f_0 signal in a straightforward linear fashion.

In practice, the relevance of the aliasing of the PSD of pulse energy fluctuations is determined by the presence of technical noise on the pulse energies at high Fourier frequency $f > f_{rep}/2N$. For sufficiently small downsampling factors (e.g. $f_{rep}/2N \leq \sim 50MHz$) and depending on the comb source, it is possible that the only source of intensity noise at frequencies above $f_{rep}/2N$ is shot noise. Shot noise results in a maximal (shot-noise-limited) signal-to-noise ratio (SNR) of an optical heterodyne beat with a local oscillator laser which is reduced by N^2 (in electrical power units) as the average power of the pulse train is reduced by downsampling by a factor of N . In contrast, in the case of detection of a carrier-envelope-offset beat with fixed optical detection bandwidth, the shot-noise-limited SNR is preserved in downsampling. One way to understand these results is to model the shot noise at a given Fourier frequency as the incoherent sum of optical heterodyne beats between each optical comb mode and the uncorrelated vacuum fluctuations at the appropriate

optical frequency [54, 55], and to take into account the fact that during downsampling the optical power of each comb mode is reduced by N^2 , with the first factor of N coming from reduction of the total optical power and the second factor of N due to the increase in the spectral density of comb modes.

We experimentally investigate the impact of downsampling on the PSD of pulse energy fluctuations by measuring noise on three photodetected optical signals: a shot-noise-limited telecom-band CW laser, a 10 GHz pulse train generated by passing this laser through cascaded optical phase and intensity modulators (see Chapter ??, [56]) and then a low-noise EDFA, and this pulse train after downsampling by a factor of four to 2.5 GHz repetition rate with no additional amplification after downsampling. Shown in Figure 2.4 are curves for each signal of the fluctuations $\sqrt{S_I(f = 50 \text{ MHz})}$ in the detected photocurrent at a Fourier frequency of 50 MHz versus the total time-averaged detected photocurrent $\langle I \rangle$ from the optical signal. To measure the scaling of noise with optical power, these curves are generated by beginning with an optical signal which yields more than 800 μA of detected photocurrent and attenuating this signal before photodetection. The data indicate that both the pulse-generation process and the downsampling process contribute some amount of technical noise at 50 MHz Fourier frequency to the photocurrent, because the measured curves are well-modeled by a quadrature sum of a shot-noise contribution and a technical noise contribution. The contributions of these two types of noise can be determined because they scale differently with the photodetected power: shot noise obeys the relationship $\sqrt{S_I(f = 50 \text{ MHz})} = \sqrt{2e \langle I \rangle}$, $\langle I \rangle$ denoting the time-averaged photocurrent, while the technical-noise contribution arises from fluctuations in the expected photocurrent $I(t)$ and scales linearly with the detected photocurrent. We observe that downsampling by a factor of four leads to a multiplication of the amplitude of the technical noise by a factor of ~ 1.7 on the optical signal relative to the carrier, which due to finite noise bandwidth is somewhat less than the factor of two (four, in electrical power units) that would be expected for ideal downsampling by a factor of four in the presence of white technical noise. These results further demonstrate that, properly implemented, downsampling does not magnify noise on the pulse train to a degree that is prohibitive for applications.

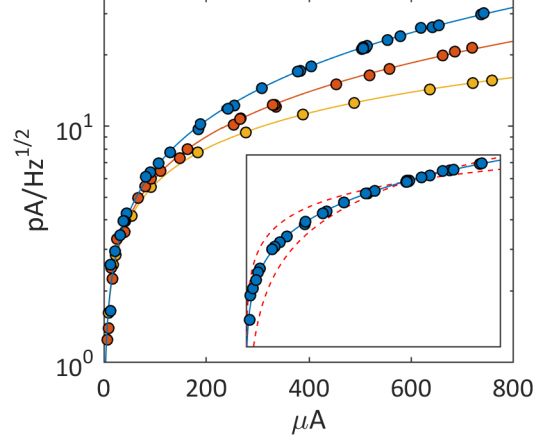


Figure 2.4: **Effect of downsampling on photocurrent fluctuations.** Fluctuations at 50 MHz Fourier frequency in the detected photocurrent as a function of the time-averaged photocurrent in three cases: CW laser at the shot-noise limit (lowest, yellow), 10 GHz pulse train (middle, red), and 2.5 GHz downsampled pulse train (highest, blue). Dots show measured data and curves show fits to the data. The fit for the shot-noise-limited laser has a single free parameter, which is a scaling factor of order 1 due to frequency dependence of the photodetector’s transimpedance gain. The fits for the pulse trains have a scaling factor in common, and have as an additional parameter the amplitude of the technical noise on the pulse train. This is -153.9 dBc/Hz for the 10 GHz pulse train and increases by a factor of ~ 1.72 to -149.3 dBc/Hz for the 2.5 GHz downsampled pulse train. Inset: Optimized fits (dashed red) to the experimental data for the downsampled 2.5 GHz pulse train using only shot noise or linear technical noise scaling, demonstrating that both noise processes are important for explaining the data.

2.5 Model for the effect of incomplete extinction of rejected pulses and amplification of a downsampled pulse train

To this point, we have considered effects of downsampling assuming that extinction of the rejected pulses is complete, but in a practical application this is not necessarily the case. The modulators used for pulse extinction may transmit a substantial amount of energy from the rejected pulses—for example, one commercial manufacturer specifies 25 dB extinction ratio, and this number vary in practice. Additionally, the electronic gating signal may not have sufficient bandwidth to completely switch from transmission to extinction within the repetition period of the incoming pulse train, and initial extinction can be followed by some transmission caused by ringing in the gating signal. Bandwidth limitations will be increasingly likely as the repetition rates of frequency combs increase, placing more demanding requirements on gating electronics. Incomplete extinction

will add modulations to the optical spectrum and will raise the total power of the downsampled pulse train while keeping the energy of the fully-transmitted pulses fixed. This will require higher average power to achieve a given target pulse energy.

The effects of incomplete extinction of rejected pulses are exacerbated if the incomplete extinction does not happen in a deterministic and repetitive fashion; this could occur, for example, if intermediate pulses fall near the edge of the gate in the presence of relative timing jitter between the optical and electronic pulse trains, or if the extinction ratio fluctuates in time. Interestingly, if the downsampled pulse train is subsequently amplified and spectrally broadened, the impact of incomplete extinction depends on whether the optical amplifier used operates in the linear regime or in the saturated regime.

As an example, we consider the case where each fully transmitted pulse is preceded and followed by partially-extinguished pulses whose amplitudes fluctuate for each period of the downsampled pulse train. This fluctuation could occur because the pulses lie on the edge of the electronic gate and there is relative timing jitter between the optical pulse train and the gating signal. It is true that these fluctuations will lead to decoherence during nonlinear spectral broadening. However, the coherence is degraded by this mechanism only within the bandwidth that is achieved by the broadened, partially-extinguished pulses. In efficient $f - 2f$ interferometry only the fully-transmitted pulses should reach an octave in bandwidth. Therefore, this mechanism of supercontinuum decoherence is not a problem in $f - 2f$ interferometry in general, unless there is coupling between the amplitudes of the amplified partially-extinguished pulses and the amplified fully-transmitted pulses. This coupling can arise, for example, through amplification in the saturation regime, which then leads to decoherence across the full bandwidth of the supercontinuum.

To illustrate this point, we have performed numerical simulations of the spectral broadening of a 100 GHz train of 100 fs pulses which has been downsampled to 10 GHz and then amplified. We use an adaptive [57] split-step Fourier method [58] to simulate spectral broadening in 30 cm of HNLF according to the generalized nonlinear Schrodinger equation [8] (see Appendix ??). In the simulation each fully-transmitted pulse, amplified to 1 nJ, is preceded and followed by partially-

extinguished pulses with normally distributed and uncorrelated energies with mean of 0.3 nJ and standard deviation of 0.225 nJ. This models the effect of adjacent pulses that coincide with the edge of the gate. We simulate amplification in two regimes: saturation is simulated using a fixed-energy method wherein the pulse energies in each three-pulse burst are rescaled by a common factor so that the total energy is 1.6 nJ; linear amplification is simulated using a fixed-gain model, which involves no such rescaling of pulses. Numerically, we simulate the spectral broadening of each pulse individually, which is acceptable because terms in the generalized nonlinear Schrodinger equation operate only locally or, in the case of the Raman term, on the timescale of several femtoseconds, while the separation between the pulses in each burst is 10 ps (the inverse of the initial 100 GHz repetition rate). We have verified that during simulated time-evolution each broadened pulse remains well-centered in its 5 ps simulation window.

Results of this study are shown in Figure 2.5. Figure 2.5a depicts a three-pulse burst before and after propagation in HNLF. In Figure 2.5b we show spectra corresponding to spectral broadening of this three-pulse burst, as well as plots of the spectral coherence averaged over many simulations. The first-order spectral coherence $g_{12}^{(1)}(\lambda)$ is defined as:

$$\left| g_{12}^{(1)}(\lambda) \right| = \left| \frac{\langle E_1^*(\lambda) E_2(\lambda) \rangle}{\sqrt{\langle |E_1(\lambda)|^2 \rangle \langle |E_2(\lambda)|^2 \rangle}} \right| = \left| \frac{\langle E_1^*(\lambda) E_2(\lambda) \rangle}{\langle |E(\lambda)|^2 \rangle} \right|. \quad (2.5)$$

Curves are plotted for the fixed-gain and fixed-energy cases, as well as for the case with ideal downsampling (no partially-extinguished pulses) and only shot-noise on the pulse train. The averages in the formula above are over 1000 instantiations of the pair E_1 and E_2 , for a total of 2000 broadened spectra for each pulse within the burst of three. In both the fixed-gain and fixed-energy cases the coherence is poor in the center of the spectrum, but in the fixed-gain case, which models amplification in the linear regime, the coherence is preserved in the high- and low-frequency ends of the spectrum where it is needed for self-referencing.

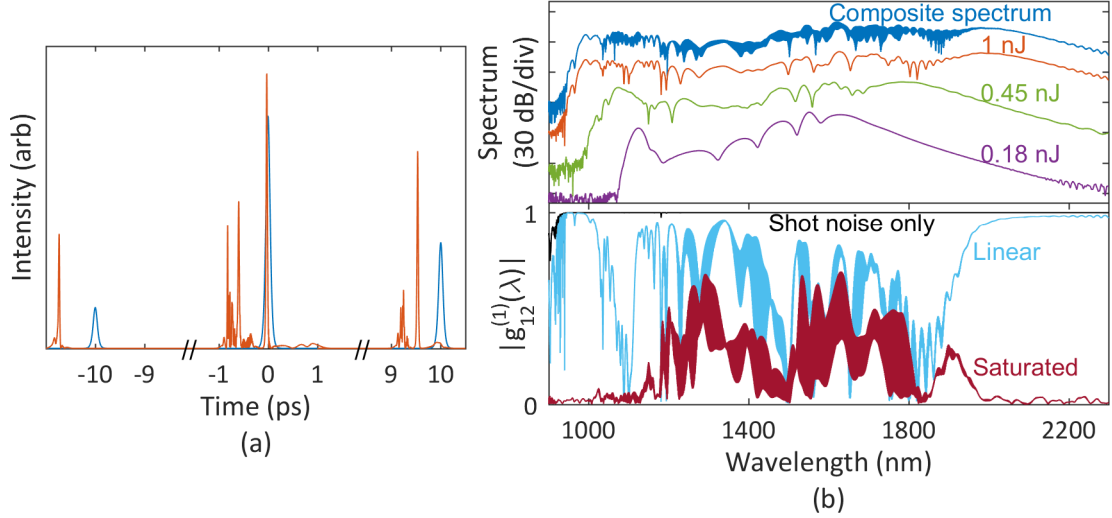


Figure 2.5: **Investigation of incomplete pulse extinction and amplification.** (a) A burst consisting of a fully-transmitted 1 nJ, 100 fs pulse and 100 fs partially-transmitted adjacent pulses with energies of 0.18 nJ and 0.45 nJ. Blue indicates initial sech^2 pulses, and orange indicates the intensity after propagation through 30 cm HNLF. Note that the x -axis has been broken. (b) Top panel: optical spectra corresponding to the pulses shown in orange in (a), showing the composite spectrum of the three pulses (top, blue) and the spectra of the 1 nJ central pulse (second, orange), the 0.45 nJ adjacent pulse (third, green), and the 0.18 nJ adjacent pulse (bottom, purple). Bottom panel: Calculated spectral coherence averaged over 2000 simulations for the case of shot noise only (top, black) and for the case of fluctuating amplitudes of the first and third pulses as described in the text, after simulated amplification in a linear-regime optical amplifier (second, teal), and a saturated optical amplifier (bottom, maroon). For the case of linear-regime operation, high spectral coherence is preserved in the extreme ends of the supercontinuum even as it is lost in the center, in contrast with the complete loss of coherence after amplification in saturation.

2.6 Further remarks on the application of downsampling

Downsampling via pulse gating is a promising tool to manipulate high-repetition-rate frequency combs from low size, weight, and power packages and to aid in the detection of their offset frequencies. In our experiments downsampling enabled detection of f_0 at a signal-to-noise ratio sufficient for measurement and stabilization, which otherwise would have required significantly higher average power. The effects of the electronic timing jitter of the gate signal are negligible so long as incoming optical pulses do not arrive coincidentally with the edge of the gate; when they do, timing jitter induces amplitude noise on the transmitted pulses. This results in an increase in RMS optical pulse energy fluctuations σ_{PEF} . Independently, the PSD of pulse energy fluctuations may be increased by aliasing of technical noise and by shot noise, depending on the relative magnitudes of these two

types of noise. Each of these sources of signal-to-noise-ratio degradation has the potential to interfere with detection of f_0 . This investigation of these challenges will facilitate application of the technique in high-repetition-rate frequency comb systems. Importantly, our experiments demonstrated that downsampling does not add a significant amount of noise to the frequency components of the pulse train, and in a separate experiment the technique has recently been used successfully to detect the carrier-envelope offset frequency of a 10 GHz comb by downsampling by a factor of four ([59], see Chapter ??).

To employ downsampling as demonstrated here with repetition rates >10 GHz will require electronic gates with duration ≤ 100 ps. Technology to downsample with gates as short as 20 ps is commercially available, while 100 Gb/s integrated circuits and 25 GHz demultiplexing have been demonstrated [60, 61]. Barring the use of such state-of-the-art electronics, pulse gates of duration longer than the incoming optical pulse train's repetition period can be employed. This will be technically easier to achieve, but will result in additional modulations on the spectrum of the downsampled pulse train.

The ambiguity of the input comb's offset frequency as a result of the reduction of the offset frequency modulo the new repetition rate makes downsampling most suitable for applications where the ambiguity can be removed by some other method. Two such applications are frequency comb calibration of astronomical spectrographs, where measurement of the wavelength of a comb mode can remove the ambiguity, and microresonator-based frequency combs, where the uncertainty in the offset frequency is determined by the frequency stability of the pump laser and can be much less than the repetition rate of the downsampled comb.

References

- [1] T. J. Kippenberg, R Holzwarth, and S. A. Diddams. Microresonator-Based Optical Frequency Combs. *Science (New York, N.Y.)*, 332 (6029), **2011**, 555–559. DOI: 10.1126/science.1193968 (cited on pages 1, 8).
- [2] A. A. Savchenkov, A. B. Matsko, and L Maleki. On Frequency Combs in Monolithic Resonators. *Nanophotonics*, 5, **2016**, 363–391. DOI: 10.1515/nanoph-2016-0031 (cited on page 1).
- [3] Y. K. Chembo. Kerr optical frequency combs: Theory, applications and perspectives. *Nanophotonics*, 5 (2), **2016**, 214–230. DOI: 10.1515/nanoph-2016-0013 (cited on page 1).
- [4] A. Pasquazi, M. Peccianti, L. Razzari, D. J. Moss, S. Coen, M. Erkintalo, Y. K. Chembo, T. Hansson, S. Wabnitz, P. Del’Haye, X. Xue, A. M. Weiner, and R. Morandotti. Micro-combs: A novel generation of optical sources. *Physics Reports*, 729, **2017**, 1–81. DOI: 10.1016/j.physrep.2017.08.004 (cited on page 1).
- [5] E. Obrzud, S. Lecomte, and T. Herr. Temporal solitons in microresonators driven by optical pulses. *Nature Photonics*, 11 (August), **2017**, 600–607. DOI: 10.1038/nphoton.2017.140. arXiv: 1612.08993 (cited on pages 1, 20).
- [6] H. Lee, T. Chen, J. Li, K. Y. Yang, S. Jeon, O. Painter, and K. J. Vahala. Chemically etched ultrahigh-Q wedge-resonator on a silicon chip. *Nature Photonics*, 6 (6), **2012**, 369–373. DOI: 10.1038/nphoton.2012.109. arXiv: 1112.2196 (cited on page 2).
- [7] K. Y. Yang, K. Beha, D. C. Cole, X. Yi, P. Del’Haye, H. Lee, J. Li, D. Y. Oh, S. A. Diddams, S. B. Papp, and K. J. Vahala. Broadband dispersion-engineered microresonator on a chip. *Nature Photonics*, 10 (March), **2016**, 316–320. DOI: 10.1038/nphoton.2016.36 (cited on page 2).
- [8] G. P. Agrawal. **Nonlinear Fiber Optics**. 4th. Burlington, MA: Elsevier, 2007 (cited on pages 2, 8, 11, 17, 33).
- [9] M. L. Calvo and V. Lakshminarayanan, eds. **Optical Waveguides: From Theory to Applied Technologies**. Boca Raton, FL: Taylor & Francis, 2007 (cited on page 2).
- [10] P. Del’Haye, S. A. Diddams, and S. B. Papp. Laser-machined ultra-high-Q microrod resonators for nonlinear optics. *Applied Physics Letters*, 102, **2013**, 221119 (cited on page 3).
- [11] A. N. Oraevsky. Whispering-gallery waves. *Quantum Electronics*, 32 (42), **2002**, 377–400. DOI: 10.1070/QE2001v031n05ABEH002205. arXiv: arXiv:1011.1669v3 (cited on page 3).

- [12] H. A. Haus. **Waves and Fields in Optoelectronics**. Englewood Cliffs: Prentice-Hall, 1984 (cited on pages 3, 4).
- [13] S. M. Spillane, T. J. Kippenberg, O. J. Painter, and K. J. Vahala. Ideality in a Fiber-Taper-Coupled Microresonator System for Application to Cavity Quantum Electrodynamics. *Physical review letters*, 91 (4), **2003**, 043902. DOI: 10.1103/PhysRevLett.91.043902 (cited on page 5).
- [14] V. S. Il'chenko and M. L. Gorodetskii. Thermal nonlinear effects in optical whispering gallery microresonators.pdf. *Laser Physics*, 2 (6), **1992**, 1004–1009 (cited on page 5).
- [15] T. Carmon, L. Yang, and K. J. Vahala. Dynamical thermal behavior and thermal self-stability of microcavities. *Optics Express*, 12 (20), **2004**, 4742–4750. URL: <http://www.ncbi.nlm.nih.gov/pubmed/19484026><http://www.opticsinfobase.org/oe/abstract.cfm?uri=oe-12-20-4742> (cited on page 5).
- [16] R. W. Boyd. **Nonlinear Optics**. San Diego, CA: Elsevier, 2003 (cited on page 7).
- [17] R. del Coso and J. Solis. Relation between nonlinear refractive index and third-order susceptibility in absorbing media. *Journal of the Optical Society of America B*, 21 (3), **2004**, 640. DOI: 10.1364/JOSAB.21.000640 (cited on page 8).
- [18] P. Del'Haye, A. Schliesser, O. Arcizet, T. Wilken, R. Holzwarth, and T. J. Kippenberg. Optical frequency comb generation from a monolithic microresonator. *Nature*, 450 (7173), **2007**, 1214–1217. DOI: 10.1038/nature06401 (cited on page 8).
- [19] T. Kippenberg, S. Spillane, and K. Vahala. Kerr-Nonlinearity Optical Parametric Oscillation in an Ultrahigh-Q Toroid Microcavity. *Physical Review Letters*, 93 (8), **2004**, 083904. DOI: 10.1103/PhysRevLett.93.083904 (cited on page 8).
- [20] A. A. Savchenkov, A. B. Matsko, D. Strekalov, M. Mohageg, V. S. Ilchenko, and L. Maleki. Low threshold optical oscillations in a whispering gallery mode CaF₂ resonator. *Physical Review Letters*, 93 (24), **2004**, 2–5. DOI: 10.1103/PhysRevLett.93.243905 (cited on page 8).
- [21] I. H. Agha, Y. Okawachi, M. A. Foster, J. E. Sharping, and A. L. Gaeta. Four-wave-mixing parametric oscillations in dispersion-compensated high-Q silica microspheres. *Physical Review A - Atomic, Molecular, and Optical Physics*, 76 (4), **2007**, 1–4. DOI: 10.1103/PhysRevA.76.043837 (cited on page 8).
- [22] F. Leo, S. Coen, P. Kockaert, S.-P. Gorza, P. Emplit, and M. Haelterman. Temporal cavity solitons in one-dimensional Kerr media as bits in an all-optical buffer. *Nature Photonics*, 4 (7), **2010**, 471–476. DOI: 10.1038/nphoton.2010.120 (cited on page 9).
- [23] T. Herr, K. Hartinger, J. Riemensberger, C. Y. Wang, E. Gavartin, R. Holzwarth, M. L. Gorodetsky, and T. J. Kippenberg. Universal formation dynamics and noise of Kerr-frequency combs in microresonators. *Nature Photonics*, 6 (7), **2012**, 480–487. DOI: 10.1038/nphoton.2012.127 (cited on page 9).
- [24] Y. K. Chembo and C. R. Menyuk. Spatiotemporal Lugiato-Lefever formalism for Kerr-comb generation in whispering-gallery-mode resonators. *Physical Review A*, 87, **2013**, 053852. DOI: 10.1103/PhysRevA.87.053852 (cited on page 9).

- [25] S. Coen, H. G. Randle, T. Sylvestre, and M. Erkintalo. Modeling of octave-spanning Kerr frequency combs using a generalized mean-field Lugiato-Lefever model. *Optics letters*, 38 (1), **2013**, 37–39. URL: <http://www.ncbi.nlm.nih.gov/pubmed/23282830> (cited on pages 9, 11, 12).
- [26] M. Haelterman, S. Trillo, and S. Wabnitz. Dissipative modulation instability in a nonlinear dispersive ring cavity. *Optics Communications*, 91 (5-6), **1992**, 401–407. DOI: 10.1016/0030-4018(92)90367-Z (cited on page 9).
- [27] T. Hansson, M. Bernard, and S. Wabnitz. Modulational Instability of Nonlinear Polarization Mode Coupling in Microresonators. 35 (4), **2018**. URL: <https://arxiv.org/pdf/1802.04535.pdf>. arXiv: arXiv:1802.04535v1 (cited on page 11).
- [28] T. Herr, V. Brasch, J. D. Jost, C. Y. Wang, N. M. Kondratiev, M. L. Gorodetsky, and T. J. Kippenberg. Temporal solitons in optical microresonators. *Nature Photonics*, 8 (2), **2014**, 145–152. DOI: 10.1109/CLEOE-IQEC.2013.6801769. arXiv: 1211.0733 (cited on pages 11, 18–20).
- [29] Y. K. Chembo, I. S. Grudinin, and N. Yu. Spatiotemporal dynamics of Kerr-Raman optical frequency combs. *Physical Review A*, 92 (4), **2015**, 4. DOI: 10.1103/PhysRevA.92.043818 (cited on page 11).
- [30] C. Godey, I. V. Balakireva, A. Coillet, and Y. K. Chembo. Stability analysis of the spatiotemporal Lugiato-Lefever model for Kerr optical frequency combs in the anomalous and normal dispersion regimes. *Physical Review A*, 89 (6), **2014**, 063814. DOI: 10.1103/PhysRevA.89.063814 (cited on pages 12, 14).
- [31] I. V. Barashenkov and Y. S. Smirnov. Existence and stability chart for the ac-driven, damped nonlinear Schrödinger solitons. *Physical Review E - Statistical Physics, Plasmas, Fluids, and Related Interdisciplinary Topics*, 54 (5), **1996**, 5707–5725. DOI: 10.1103/PhysRevE.54.5707 (cited on pages 12, 18).
- [32] A. Coillet and Y. K. Chembo. Routes to spatiotemporal chaos in Kerr optical frequency combs. *Chaos*, 24 (1), **2014**, 5. DOI: 10.1063/1.4863298. arXiv: arXiv:1401.0927v1 (cited on page 15).
- [33] L. A. Lugiato and R. Lefever. Spatial Dissipative Structures in Passive Optical Systems. *Physical Review Letters*, 58 (21), **1987**, 2209–2211 (cited on page 15).
- [34] L. Lugiato and R. Lefever. Diffraction stationary patterns in passive optical systems. *Interaction of Radiation with Matter*, **1987** (cited on page 15).
- [35] W. H. Renninger and P. T. Rakich. Closed-form solutions and scaling laws for Kerr frequency combs. *Scientific Reports*, 6 (1), **2016**, 24742. DOI: 10.1038/srep24742. arXiv: 1412.4164 (cited on page 15).
- [36] X. Yi, Q.-F. Yang, K. Y. Yang, M.-G. Suh, and K. Vahala. Soliton frequency comb at microwave rates in a high-Q silica microresonator. *Optica*, 2 (12), **2015**, 1078–1085 (cited on pages 18, 20).

- [37] S. Coen and M. Erkintalo. Universal scaling laws of Kerr frequency combs. *Optics letters*, 38 (11), **2013**, 1790–1792. DOI: 10.1364/OL.38.001790. arXiv: arXiv:1303.7078v1 (cited on page 18).
- [38] V. Brasch, T. Herr, M. Geiselmann, G. Lihachev, M. H. P. Pfeiffer, M. L. Gorodetsky, and T. J. Kippenberg. Photonic chip-based optical frequency comb using soliton Cherenkov radiation. *Science*, 351 (6271), **2016**, 357. DOI: 10.1364/CLEO_SI.2015.STh4N.1. arXiv: 1410.8598 (cited on page 20).
- [39] V. E. Lobanov, G. V. Lihachev, N. G. Pavlov, A. V. Cherenkov, T. J. Kippenberg, and M. L. Gorodetsky. Harmonization of chaos into a soliton in Kerr frequency combs. *Optics Express*, 24 (24), **2016**, 27382. DOI: 10.1126/science.aah4243. arXiv: 1607.08222 (cited on page 20).
- [40] J. K. Jang, M. Erkintalo, S. G. Murdoch, and S. Coen. Writing and erasing of temporal cavity solitons by direct phase modulation of the cavity driving field. *Optics Letters*, 40 (20), **2015**, 4755–4758. DOI: 10.1364/OL.40.004755. arXiv: 1501.05289 (cited on page 20).
- [41] J. K. Jang, M. Erkintalo, S. Coen, and S. G. Murdoch. Temporal tweezing of light through the trapping and manipulation of temporal cavity solitons. *Nature Communications*, 6, **2015**, 7370. DOI: 10.1038/ncomms8370. arXiv: 1410.4836 (cited on page 20).
- [42] Y. Wang, B. Garbin, F. Leo, S. Coen, M. Erkintalo, and S. G. Murdoch. Writing and Erasure of Temporal Cavity Solitons via Intensity Modulation of the Cavity Driving Field. *arXiv*, **2018**, 1802.07428. arXiv: 1802.07428 (cited on page 20).
- [43] H. Taheri, A. A. Eftekhari, K. Wiesenfeld, and A. Adibi. Soliton formation in whispering-gallery-mode resonators via input phase modulation. *IEEE Photonics Journal*, 7 (2), **2015**, 2200309. DOI: 10.1109/JPHOT.2015.2416121 (cited on page 21).
- [44] S. B. Papp, K. Beha, P. Del’Haye, F. Quinlan, H. Lee, K. J. Vahala, and S. A. Diddams. Microresonator frequency comb optical clock. *Optica*, 1 (1), **2014**, 10–14. DOI: 10.1364/OPTICA.1.000010. arXiv: 1309.3525 (cited on page 21).
- [45] D. T. Spencer, T. Drake, T. C. Briles, J. Stone, L. C. Sinclair, C. Fredrick, Q. Li, D. Westly, B. R. Ilic, A. Bluestone, N. Volet, T. Komljenovic, L. Chang, S. H. Lee, D. Y. Oh, T. J. Kippenberg, E. Norberg, L. Theogarajan, M.-g. Suh, K. Y. Yang, H. P. Martin, K. Vahala, N. R. Newbury, K. Srinivasan, J. E. Bowers, S. A. Diddams, and S. B. Papp. An optical-frequency synthesizer using integrated photonics. *Nature*, 557, **2018**, 81–85. DOI: 10.1038/s41586-018-0065-7 (cited on page 21).
- [46] S. Backus, C. G. Durfee, M. M. Murnane, and H. C. Kapteyn. High power ultrafast lasers. *Review of Scientific Instruments*, 69 (3), **1998**, 1207. DOI: 10.1063/1.1148795 (cited on page 22).
- [47] A. Baltuska, M. Uiberacker, E. Goulielmakis, R. Kienberger, V. S. Yakovlev, T. Udem, T. W. Hänsch, and F. Krausz. Phase-Controlled Amplification of Few-Cycle Laser Pulses. *IEEE Journal of Selected Topics in Quantum Electronics*, 9 (4), **2003**, 972–989 (cited on page 22).

- [48] C. Gohle, J. Rauschenberger, T. Fuji, T. Udem, A. Apolonski, F. Krausz, and T. W. Hänsch. Carrier envelope phase noise in stabilized amplifier systems. 30 (18), **2005**, 2487–2489 (cited on pages 23, 30).
- [49] J. Rauschenberger, T. Fuji, M. Hentschel, A.-J. Verhoef, T. Udem, C. Gohle, T. W. Hänsch, and F. Krausz. Carrier-envelope phase-stabilized amplifier system. *Laser Physics Letters*, 3 (1), **2006**, 37–42. DOI: 10.1002/lap1.200510053 (cited on page 23).
- [50] M. E. Fermann, V. I. Kruglov, B. C. Thomsen, J. M. Dudley, and J. D. Harvey. Self-similar propagation and amplification of parabolic pulses in optical fibers. *Physical review letters*, 84 (26 Pt 1), **2000**, 6010–3. URL: <http://www.ncbi.nlm.nih.gov/pubmed/10991111> (cited on page 24).
- [51] M. Hirano, T. Nakanishi, T. Okuno, and M. Onishi. Silica-Based Highly Nonlinear Fibers and Their Application. *Sel. Top. Quantum Electron.*, 15 (1), **2009**, 103–113. DOI: 10.1109/JSTQE.2008.2010241 (cited on page 24).
- [52] D. Mandridis, I. Ozdur, F. Quinlan, M. Akbulut, J. J. Plant, P. W. Juodawlkis, and P. J. Delfyett. Low-noise, low repetition rate, semiconductor-based mode-locked laser source suitable for high bandwidth photonic analog – digital conversion. *Applied Optics*, 49 (15), **2010**, 2850–2857 (cited on page 27).
- [53] J. M. Dudley, G. G. Genty, and S. Coen. Supercontinuum generation in photonic crystal fiber. *Reviews of Modern Physics*, 78 (4), **2006**, 1135–1184. DOI: 10.1103/RevModPhys.78.1135 (cited on page 27).
- [54] H.-A. Bachor and P. J. Manson. Practical Implications of Quantum Noise. *Journal of Modern Optics*, 37 (11), **1990**, 1727–1740. DOI: 10.1080/09500349014551951 (cited on page 31).
- [55] F. Quinlan, T. M. Fortier, H. Jiang, and S. a. Diddams. Analysis of shot noise in the detection of ultrashort optical pulse trains. *Journal of the Optical Society of America B*, 30 (6), **2013**, 1775. DOI: 10.1364/JOSAB.30.001775 (cited on page 31).
- [56] D. C. Cole, K. M. Beha, S. A. Diddams, and S. B. Papp. Octave-spanning supercontinuum generation via microwave frequency multiplication. *Proceedings of the 8th Symposium on Frequency Standards and Metrology 2015, Journal of Physics: Conference Series*, 723, **2016**, 012035. DOI: 10.1088/1742-6596/723/1/012035 (cited on page 31).
- [57] A. M. Heidt. Efficient Adaptive Step Size Method for the Simulation of Supercontinuum Generation in Optical Fibers. *Journal of Lightwave Technology*, 27 (18), **2009**, 3984–3991 (cited on page 33).
- [58] J. Hult. A Fourth-Order Runge-Kutta in the Interaction Picture Method for Simulating Supercontinuum Generation in Optical Fibers. *Journal of Lightwave Technology*, 25 (12), **2007**, 3770–3775. DOI: 10.1109/JLT.2007.909373 (cited on page 33).
- [59] K. Beha, D. C. Cole, P. Del’Haye, A. Coillet, S. A. Diddams, and S. B. Papp. Electronic synthesis of light. *Optica*, 4 (4), **2017**, 406–411. DOI: 10.1364/OPTICA.4.000406 (cited on page 36).

- [60] R. Driad, J. Rosenzweig, R. E. Makon, R. Lösch, V. Hurm, H. Walcher, and M. Schlechtweg. InP DHBT-Based IC Technology for 100-Gb / s Ethernet. *IEEE Trans. on Electron. Devices*, 58 (8), **2011**, 2604–2609 (cited on page 36).
- [61] D. Ferenci, M. Grozing, M. Berroth, R. Makon, R. Driad, and J. Rosenzweig. A 25 GHz Analog Demultiplexer with a Novel Track and Hold Circuit for a 50 GS / s A / D-Conversion System in InP DHBT Technology. In: **Microwave Symposium Digest**. 2012, pp. 1–3 (cited on page 36).